Constraints on the low-energy $E1$ cross section of $^{12}C(\alpha,\gamma)^{16}O$ from the β-delayed α spectrum of ^{16}N

R.E. Azuma,[1] L. Buchmann,[2] F.C. Barker,[3] C.A. Barnes,[4] J.M. D'Auria,[5] M. Dombsky,[5,6] U. Giesen,[1,2] K.P. Jackson,[2,5] J.D. King,[1] R.G. Korteling,[5] P. McNeely,[6] J. Powell,[1] G. Roy,[6] J. Vincent,[2] T.R. Wang,[1,4] S.S.M. Wong,[1] and P.R. Wrean[4]

[1] *Department of Physics, University of Toronto, Toronto, Ontario, Canada M5S 1A7*

[2] *TRIUMF, 4004 Wesbrook Mall, Vancouver, British Columbia, Canada V6T 2A3*

[3] *Department of Theoretical Physics, Research School of Physical Sciences and Engineering, Australian National University, Canberra, Australian Capital Territory 0200, Australia*

[4] *W.K. Kellogg Laboratory, California Institute of Technology, Pasadena, California 91125*

[5] *Department of Chemistry, Simon Fraser University, Burnaby, British Columbia, Canada V5A 1S6*

[6] *Department of Physics, University of Alberta, Edmonton, Alberta, Canada T6G 2J1*

(Received 16 March 1994)

The shape of the low-energy part of the β-delayed α-particle spectrum of ^{16}N is very sensitive to the $\alpha+^{12}C$ reduced width of the 7.117 MeV subthreshold state of ^{16}O. This state, in turn, dominates the low-energy p-wave capture amplitude of the astrophysically important $^{12}C(\alpha,\gamma)^{16}O$ reaction. The α spectrum following the decay of ^{16}N has been measured by producing a low-energy $^{16}N^{14}N^{+}$ beam with the TRIUMF isotope separator TISOL, stopping the molecular ions in a foil, and counting the α particles and ^{12}C recoil nuclei in coincidence, in thin surface-barrier detectors. In addition to obtaining the α spectrum, this procedure determines the complete detector response including the low-energy tail. The spectrum, which contains more than 10^6 events, has been fitted by R- and K-matrix parametrizations which include the measured $^{12}C(\alpha,\gamma)^{16}O$ cross section and the measured $\alpha+^{12}C$ elastic-scattering phase shifts. The model space appropriate for these parametrizations has been investigated. For $S_{E1}(300)$, the $E1$ part of the astrophysical S factor for the $^{12}C(\alpha,\gamma)^{16}O$ reaction at $E_{c.m.} = 300$ keV, values of 79 ± 21 and 82 ± 26 keV b have been derived from the R- and K-matrix fits, respectively.

PACS number(s): 95.30.Cq, 23.60.+e, 27.20.+n

I. INTRODUCTION

The helium-burning phase of stellar evolution consists essentially of only the 3 $^4He \rightarrow {}^{12}C+\gamma$ and $^{12}C(\alpha,\gamma)^{16}O$ reactions because of the absence of appropriate states (resonances) near the $^{16}O+\alpha$ threshold. Numerous studies have shown that the ratio of the cross sections for the two reactions, and the resultant $^{12}C/^{16}O$ abundance ratio, are important in the evolution of massive stars, both for the abundances of heavier elements subsequently produced, and for determining the nature of the remnant when the stars explode as supernovas [1,2]. In particular, a small $^{12}C/^{16}O$ ratio leads to the formation of a more massive iron core during the presupernova stages, and thus increases the probability of leaving a black-hole remnant instead of a neutron star [2].

Although the "triple-α" reaction rate cannot be determined directly in the laboratory, the various factors that enter the rate have been measured, and the predicted rate at the usual helium-burning temperatures ($\sim 2 \times 10^8$ K) is believed to be known to about 15% [3]. Unfortunately, the same cannot be claimed for the rate of $^{12}C(\alpha,\gamma)^{16}O$, and it is highly desirable to know this rate with comparable accuracy to that of the triple-α process in order to test stellar evolution theory quantitatively.

The particular reasons for the great difficulty in obtaining a reliable estimate of the $^{12}C(\alpha,\gamma)^{16}O$ rate follow: (1) the cross section is needed in the neighborhood of center-of-mass energy $E = 300$ keV (the "most effective energy at 2×10^8 K"), where the cross section is smaller by a factor of more than 10^7 than it is at the lowest energy for which laboratory measurements have been possible thus far ($E \sim 1$ MeV)[1]; and (2) at 300 keV, the cross section depends mainly on the properties of two ^{16}O states below the $^{12}C+\alpha$ threshold (subthreshold levels)—a $J^\pi = 1^-$ state at an energy of -45 keV and a 2^+ state at -245 keV, to which current laboratory measurements are only weakly sensitive. Measurements are, instead, dominated by electric dipole ($E1$) contributions from a broad 1^- state at 2.42 MeV, and by direct electric-quadrupole ($E2$) radiative capture. A partial energy level diagram for ^{16}O is given in Fig. 1. In spite of many measurements [5–11], the $^{12}C(\alpha,\gamma)^{16}O$ cross section, extrapolated to 300 keV, is uncertain by more than 2 orders of magnitude, even when the extrapolation employs both the $^{12}C(\alpha,\alpha)$ elastic scattering and the capture measurements. The extrapolated (α,γ) cross section is normally expressed in terms of the astrophysical S factor [see Eq. (3) in Sec. III C].

[1] In this paper, all energies are in the $^{12}C+\alpha$ center-of-mass system unless otherwise stated.

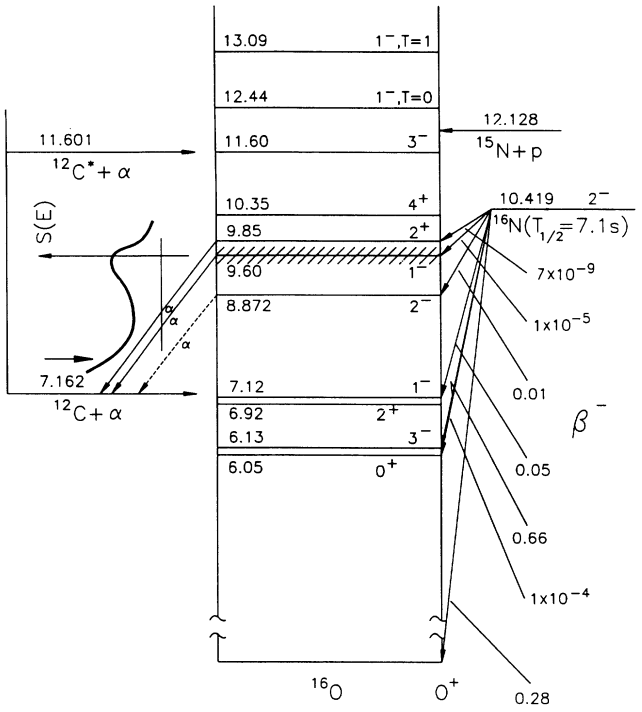

FIG. 1. Partial energy-level diagram for ^{16}O (adapted from [4]).

Because the early measurements [5–7] of the cross section were carried out with very small beam currents, they could not be extended to a low enough energy to determine the $E2/E1$ cross section ratio where it would be sensitive to the subthreshold 2^+ state. However, the possible influence of this state was anticipated in Ref. [7]. A later measurement [8] carried out in close geometry with much larger beam currents showed evidence for an appreciable $E2$ contribution. The $E2/E1$ ratio can be obtained from γ-ray angular distributions, which are less susceptible to error than absolute cross section measurements. In fact, recent measurements of the energy dependence of σ_{E2}/σ_{E1} agree much better with one another than the separate extrapolated cross sections [9,11]. This raises the possibility that a better method of determining either the $E1$ or the $E2$ cross section could be supplemented by improved values of σ_{E2}/σ_{E1} to provide a better answer to the stellar $^{12}\mathrm{C}(\alpha,\gamma)^{16}\mathrm{O}$ cross section problem. On the other hand, extending this ratio down to 300 keV still requires separate $E1$ and $E2$ cross section extrapolations.

The β-delayed α-particle spectrum from ^{16}N ($t_{1/2}$ = 7.13 s) provides a complementary route to the determination of the $E1$ cross section at low energies [12,13]. It was recognized from the outset that the ^{16}N route had major advantages over the $^{12}\mathrm{C}(\alpha,\gamma)$ route alone. The β-decay matrix element to the subthreshold 1^- state is an order of magnitude larger than that to the E_x = 9.59 MeV (E = 2.42 MeV) 1^- state, and the increasing $(\beta+\nu)$ phase space as E is lowered also helps to emphasize the low-energy region. Further, the first high-resolution β-delayed α spectra showed that high α yields, and thus good statistical accuracy, could be obtained [14,15].

Interest in the β-delayed α spectrum was renewed recently when it was shown [16–18] that the main peak in the p-wave α spectrum, due to the broad E_x = 9.59 MeV state, should be accompanied by a low-energy interference peak which is due to the "ghost" of the subthreshold E_x = 7.117 MeV state interfering destructively with the tail of the E_x = 9.59 MeV state. Both the magnitude of this secondary interference peak and the precise form of the low-energy side of the main peak were predicted to be well correlated with the reduced α width of the subthreshold state and, therefore, directly related to the $E1$ cross section.

The situation is somewhat complicated by the presence of an f-wave component in the α-decay spectrum due to the allowed β decay to nearby 3^- states. The p- and f-wave components contribute incoherently to the α spectrum.

We have carried out a new set of measurements of the α-particle spectrum extended to cover a wide energy range. We have used the TISOL facility at TRIUMF to produce a beam of ^{16}N ions that was implanted into a very thin collector foil. The α decay of ^{16}O was observed, both in singles and in α-^{12}C coincidences, with very thin detectors. The use of thin α sources and very thin detectors, as well as α-^{12}C coincidences, provided the means to obtain an α particle spectrum essentially free of background and distortion over the entire energy range, including the expected interference peak region. In addition, an empirical determination of the complete detector response function, including the low-energy tail of degraded α particles, was possible. The latter phenomenon is often ignored but becomes important here because the broad α-particle group, corresponding to the E = 2.42 MeV state, is 3 orders of magnitude more intense than the low-energy interference maximum.

A preliminary account of the present work has been published [19], as has a preliminary account of an independent study of the ^{16}N β-delayed α spectrum [20].

The following sections discuss the design of the experiment, the data acquisition, the data analysis, R- and K-matrix fits to the data, the results of these fits, and the conclusions that can be drawn.

II. EXPERIMENTAL CONSIDERATIONS

A. General

In measuring the α-particle spectrum of ^{16}N down to the low energies and yields of the interference-peak region, several difficulties are encountered. The first concern is the expected large β-ray background. Since the overall α-particle yield is only 10^{-5} that of the β-particle yield, and the interference peak in the α-particle spectrum is expected to be only about 10^{-3} as large as the main peak, reduction of β background is crucial. This was achieved with the use of very thin (10.6–15.8 μm) silicon surface-barrier detectors. The detectors were cho-

sen to be as thin as possible to reduce energy deposition by the β particles, while still stopping α particles up to the 2.5 MeV permitted by the ^{16}N β-decay Q value.

Another concern was that the spectrum of recoiling ^{12}C particles might overlay the lower part of the interference peak (see Fig. 4 in Sec. II D 1). However, the pulse-height defect is greater for ^{12}C ions than for α particles, as is the energy loss in the gold entrance window (40 μg/cm^2) and carbon collector foil (10 μg/cm^2). This leads to the carbon peak obscuring less of the interference peak than initially expected.

The contribution of degraded α particles to the α-particle spectrum at low energies is of particular concern. There are two major effects that produce a low-energy tail in the response function. The first is energy loss due to multiple scattering and straggling in the implanted source; the second is energy loss due to the same effects in the detector. Even with very thin sources, the total number of particles in the tail can be of the order of 1%. In the case of ^{16}N $\beta\alpha$ decay, a 1% tail from the main, high-energy α peak due to the broad 9.59 MeV state would produce a background below 1000 keV, approximately equal in magnitude to the expected α-particle interference peak. The large corrections required to account for the underlying tail would significantly increase the uncertainty in the resulting low-energy data. Of the techniques available to isolate these unwanted contributions, the one chosen was a method in which the α particles were detected in coincidence with their recoil ^{12}C decay partners.

In the α decay of ^{16}O the two decay products are emitted at 180° with an energy ratio of $E_\alpha/E_{^{12}C} = 3.0$ (neglecting small β and neutrino recoil effects). The signature of an acceptable event is, therefore, a back-to-back coincidence with the appropriate energy ratio. The detection of the very low-energy ^{12}C particles ($E_{^{12}C} \geq 200$ keV) that is required for this technique to be successful imposes a stringent limitation on the permitted thickness of the collector foil. The use of thin collector foils has the additional benefit of minimizing the contribution of the source thickness to energy-loss distortions of the α spectrum and minimizing the corrections required in the energy calibration of the system.

Since the available decay energy is divided between the α and ^{12}C particles in the ratio 3:1, this ratio can be used to label good events. As the α and ^{12}C absorption processes are independent, α-particle tail events should generally be accompanied by full-energy ^{12}C events. Thus, the observed energy ratio should be significantly less than 3:1, allowing a means of separating the degraded α particles from true low-energy events. The degree to which this can be done depends on the energy resolution of the system, especially for the ^{12}C recoil particles. In addition, taking data in coincidence strongly reduces the ^{12}C, β, and other backgrounds in the α-particle spectrum. The random coincidence rate will be small as the event rate is low, and true ^{12}C-β and α-β coincidences will mostly have the wrong energy ratio.

A difficulty with the coincidence requirement is the need to detect very low-energy ^{12}C particles. These ions initially have only 1/3 the energy of the corresponding α particles and suffer greater energy losses and scattering due to their higher charge. This could lead to a drop in coincidence efficiency at lower energies (see Sec. II D 6).

Both singles and coincidence spectra were recorded during the run. With a separation of about 8–10 mm between the detectors of a given coincidence pair (see Sec. II B 2), the effective solid angles subtended by the detectors were slightly sensitive to variations in the beam optics of the implantation. This was observed as minor changes in the ratio of the singles-to-coincidence counting rates and as minor variations in the positions of the peaks in the singles spectra.

The data were collected over a period of 6 weeks with individual runs of 3–6 h duration. Periodic 2-h runs with ^{18}N were taken for energy calibration purposes. All known β-particle decaying isotopes up to $A = 34$ were also checked to see whether their decay spectra could produce significant contributions to the spectrum (see Sec. II D 4) and a new β-delayed α decay was found (^{17}N).

B. Experimental setup

1. The production of ^{16}N

The experiment was carried out using the thick-target, on-line isotope separator TISOL [21–23]. A beam of 500 MeV protons with an intensity of up to 1.5 μA was extracted from the TRIUMF cyclotron and used to irradiate a thick (13 g/cm^2) target of zeolite (13X/NaAlSiO$_4$) in the form of small pellets. The zeolite was outgassed in its cylindrical steel oven by slow uniform heating to about 600 °C under vacuum for several days. During production runs the proton beam continuously provided more localized heating and further outgassing. Yields of ^{16}N of the order of 10^6/s were obtained.

Magnetic mass analysis was used to select the mass of interest from the extracted ion beam. An extraction voltage of 12 kV was used to implant the ions into the self-supporting, carbon collector foils (10 μg/cm^2). The ^{16}N appeared predominantly at mass positions 16 (^{16}N$^+$), 30 (^{16}N^{14}N$^+$), and 32 (^{16}N^{16}O$^+$). However, zeolite releases abundant yields of other light nuclides [22]. At mass 16, ^{18}N from the doubly charged ^{18}N^{14}N^{2+} molecule was observed; at mass 32, ^{18}N from ^{18}N^{14}N$^+$ was present. To minimize stable-nuclear beam current and ^{18}N contamination, mass position 30 was chosen for the production runs. Typical stable-ion beam current at mass 30 (NO$^+$) was 15 μA. Under such bombardment, the collector foils survived for periods of 10–25 h.

During the runs the β-α decay yield of ^{16}N was monitored continuously at the experimental end station (Sec. II B 2) as an indicator of the relative yield. Singles (coincidence) rates of 3–5 (1-2) events/s were observed for the summed detector pairs.

2. Detector end station

A schematic diagram of the detector end station is shown in Fig. 2. The carbon collector foils were mounted

on the vanes of a wheel which could be rotated, by means of a stepping motor, to bring the implanted activity to a position between a pair of closely spaced (8–10 mm) surface-barrier detectors. Three counting positions were located at 90°, 180°, and 270°, with respect to the beam-implantation position, with pairs of detectors at each position (D1 and D2, D3 and D4, and D5 and D6, respectively). The detectors were thin (10.6–15.8 μm) transmission-mounted, silicon surface-barrier detectors, each with an active area of 50 mm^2.

After a 3 s implantation time, chosen to maximize the count rate summed over the detector pairs, the wheel was rotated through 90° in 0.25 s, transferring the collected ^{16}N to a position between the first set of detectors. Each implanted foil was counted at three positions before being returned to 0° for further implantation. A collimator of 8.0 mm diameter limited the implantation region on the foils, whose diameters were 10.0 mm. The collimator formed an integral part of a liquid-nitrogen-cooled trap which effectively inhibited buildup of carbon on the collector foils. An einzel lens was located immediately in front of the collimator to enhance transmission of the beam to the foils.

Ion-source voltage breakdown and ion-beam-current fluctuations were sources of electronic noise in the detectors. This could lead to false coincidences since multiple detectors were affected. Noise events were usually registered in several detectors, while true coincidences could affect only one pair. Software gates were used to eliminate events where two or more detectors from different pairs registered a pulse height greater than a set threshold. This threshold was below the pulse height of the lowest energy ^{12}C ions detected, but as high as possible to decrease the loss of good events due to random coincidences with β particles.

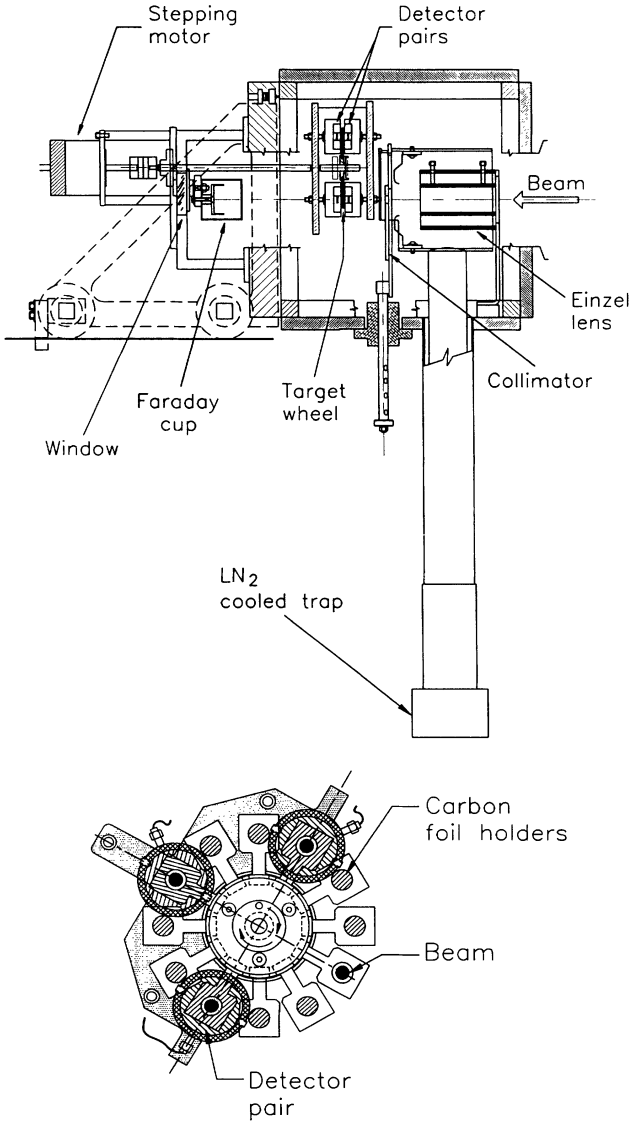

FIG. 2. Top—diagram of the target chamber assembly in the plane containing the beam. Bottom—target wheel showing the implantation foils and detector locations.

3. *Energy absorption and stopping of ions*

The implantation of ^{16}N ions into ^{12}C has been simulated with the Monte Carlo program TRIM [24]. For 12 keV ^{16}N^{14}N ions, the ^{16}N implantation depth is 3.8 μg/cm^2 with a half-width of the profile of 3.5 μg/cm^2. The same program was used to investigate the contribution of straggling of α particles and ^{12}C ions in the carbon foil to the energy resolution. The simulation showed that passage through about 6 μg/cm^2 of carbon has a negligible effect on the energy resolution and that the ^{12}C spectrum should undergo only minor distortion due to scattering in the carbon foil.

C. Electronics and data acquisition

The essential features of the electronics and data acquisition system are illustrated in Fig. 3. The objective was to record the α-particle spectra both in singles and in coincidence with ^{12}C recoil nuclei in the opposite detector. The challenge was to demonstrate a high coincidence efficiency for the detection of ^{12}C recoils emitted with energies as low as 200 keV.

The detectors were electrically isolated from the support structure and connected by coaxial cables of minimum length to vacuum feedthroughs in the plastic plate

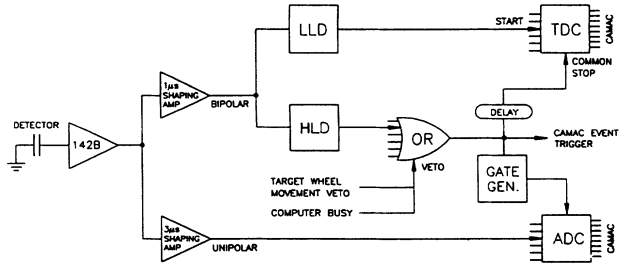

FIG. 3. Schematic of the electronics and data acquisition system.

that supported the detector mounts, stepping motor, and Faraday cup. Preamplifiers (Ortec 142B) were mounted as close as possible to the vacuum feedthroughs to keep noise contributions to a minimum. Also, to optimize the observed energy resolution, the network protecting the first stage of the preamplifier from large transient signals was disconnected. A precision pulser was used to estimate electronic noise, assist in energy calibration, and monitor changes in electronic gain. Signals from the pulser were presented (at the rate of 1 Hz) at the test input of each preamplifier throughout the experiment.

Each preamplifier was connected to two main amplifiers. The unipolar output of one amplifier provided the energy signal to the ADC with a shaping time of 3 μs. A timing signal was derived from the zero crossing of a 1 μs signal from the second amplifier. This signal occurred well before the time of maximum amplitude for the energy signal and was used in generating the gate for the ADC. The output of each (timing) amplifier was fed to two discriminators with one set at a very low level for timing purposes, and the other at a somewhat higher level for use in the master trigger.

The threshold on the higher-level discriminator (HLD) was set to a value corresponding to an α-particle energy of at most 300 keV. This was low enough to accept any α particle of interest and high enough to exclude all but a few events per second arising from the combined effects of electronic noise and the intense flux of β particles. As indicated in Fig. 3, the outputs of all six HLD's were combined in a logical OR circuit to provide a master trigger for the data acquisition. This signal opened the gate for all ADC channels which were subsequently read out via CAMAC protocol. This procedure ensured that, for detectors registering coincident low-energy recoils, the ADC was interrogated whether or not the recoil signal triggered an HLD.

The lower-level discriminators (LLD) were used to monitor the time difference between the detection of an α particle and the coincident recoil nucleus in order to assess the possible contribution of random coincidences. The thresholds were set at a level equivalent to an α-particle energy of typically 50 keV. The output of each LLD provided the start pulse for a TDC with a time range of about 1500 ns. The common stop for all ADC's was provided by the master trigger delayed by about 800 ns. In addition to the ADC readout, this trigger was followed by the readout of any TDC channels with nonzero content. For events in which both an α particle and a recoil nucleus triggered the LLD's, the time difference was estimated from the two TDC values. The average coincidence resolving times were less than 150 ns (FWHM). In all cases the rate of random coincidences was found to be negligible. As a consequence, the time spectra were not used in the analysis and the final spectra were not influenced by the operation of the LLD's.

Events were monitored on-line and stored on magnetic tape in event-by-event mode for analysis off line. As shown in Fig. 3, master trigger events were vetoed during "computer busy" signals. Since operation of the stepping motor responsible for the rotation of the wheel caused some electrical noise in the detectors, data acquisition was also disabled while the wheel was in motion. The time distribution for events associated with the β decay was monitored by sampling a clock started each time the motion of the target wheel was stopped.

In addition to the six detectors mentioned in Sec. II B 2, a thick (500 μm) silicon surface-barrier detector (D7) was mounted directly behind detector D1. During the extended periods of acquisition of the ^{16}N data, the singles counting rate in this detector was a useful monitor of the rate of β decay and hence of the performance of the isotope separator. In addition, as outlined in Sec. II D 6, this detector was used to detect the β-delayed protons emitted from selected isotopes for background determination and calibration purposes.

D. Data analysis and results

1. Singles spectrum

The singles spectrum of detector D1 is shown in Fig. 4; noise events have been removed as described in Sec. II B 2. Beginning from the high-energy end of the spectrum, the following features are apparent: above the main α peak, some events from the $\beta\alpha$ decay of ^{18}N (see Sec. II D 4) superimposed on a constant background (≈ 3 events/20 keV); the main α peak; at $E_\alpha = 1.081$ MeV, the most prominent peak from the β-delayed α decay of ^{18}N (visible only in D1 and D2 because of the short half-life); a relatively flat region containing real α events as well as events from the response tail; the ^{12}C main peak at about 1/4 the energy of the main α peak; and the high-energy end of the β-particle distribution.

As mentioned in Sec. II C, initiation of wheel rotation also started a clock so that the time distribution of events could be measured and the half-lives of events in different energy regions of the spectrum deduced. Figure 5 shows the decay curve for events in the region of the

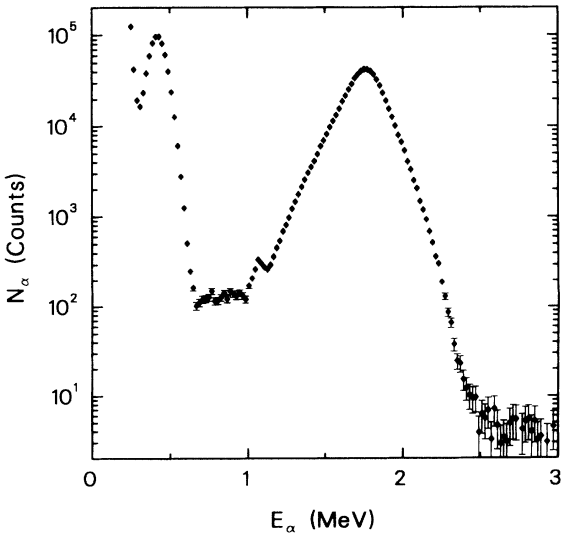

FIG. 4. Singles spectrum of detector D1. The energy calibration is for α particles. The bin width is 20 keV.

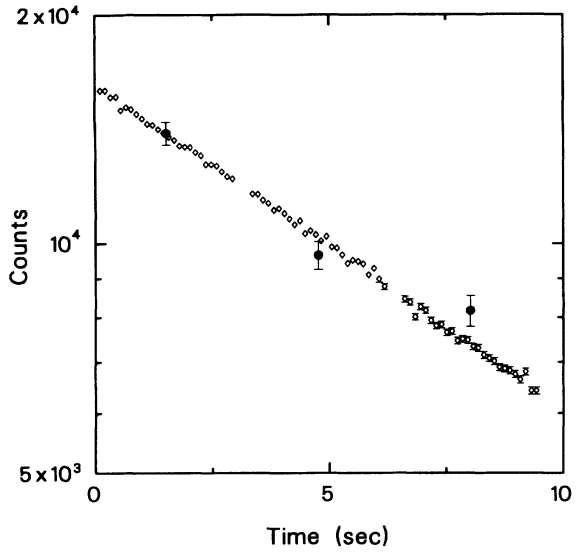

FIG. 5. Time dependence of the interference-peak events (full circles) normalized to and superimposed on the decay curve for the main α peak (open diamonds).

main peak and in the region of the interference peak for the coincidence conditions discussed in Sec. II D 3. The fitted half-life of 7.25±0.10 s is in agreement with the known half-life of 7.13±0.02 s [4] for ^{16}N.

2. *Energy calibration and resolution*

Calibration of the α-particle energy scale of the detectors was accomplished using the $\beta\alpha$-decay lines of ^{18}N (E_α = 1.081 ± 0.001 and 1.409 ± 0.001 MeV)[2] and of ^{20}Na (E_α = 2.150 ± 0.002 and 2.477 ± 0.003 MeV),[3] and the 3.182 MeV α-decay line of ^{148}Gd. Beams of ^{18}N and ^{20}Na were obtained from the TISOL facility and their decay products were observed under conditions identical to those for the α-particle spectra of ^{16}N, thus averting the need for additional corrections. For the ^{148}Gd calibration point, the source thickness was determined and the energy loss of the α particles was found to be equivalent to the loss that would have been incurred had the source been embedded in a 10μg/cm^2 carbon foil. In addition, the source-to-detector distance was chosen to subtend approximately the same solid angle as that for the α particles in the ^{16}N coincidence experiment.

The electronic resolution of the detector and amplifier system was measured by the precision pulser to be about 17 keV full width at half maximum (FWHM). Individual detector resolutions varied by ±3 keV from this average. The width of the 3.182 MeV α-decay peak from a ^{148}Gd source placed in the position noted above was 25 keV FWHM, again varying with detector by ±3 keV. The two ^{18}N β-delayed α-decay lines at 1.081 and 1.409 MeV had resolutions of about 48 keV. (The peaks are broadened by β- and ν-recoil effects.)

The energy of β-delayed particles is affected by the recoil momentum of the excited daughter nucleus. While the actual recoil energy is negligible, the momentum is sufficient to alter the energy distribution between the two products of the second decay. This causes an additional spread in the α-particle energies of ^{16}N and ^{18}N [26]. The size and shape of this spread depends on the available β energy, the α energy, and the relative angular correlation between the emitted particles. In the case of ^{16}N, where the angular correlation is known from the pure Gamow-Teller nature of the decay, this effect has been calculated. The maximum energy spread is about 15 keV FWHM and the shape of the spread is roughly Gaussian. To obtain the full energy resolution for ^{16}N α particles, this effect must be added in quadrature with the detector resolution as determined by the ^{148}Gd source. This gives a maximum ^{16}N α resolution of 30 ± 5 keV.

The ^{18}N α lines at 1.081 and 1.409 MeV provide a check of our calculation. As these lines may result from mixed Fermi and Gamow-Teller β transitions, the exact angular correlation is unknown. However, the calculated energy spread for the case that the Gamow-Teller part dominates (39 and 43 keV FWHM, respectively, for the two lines) is consistent with the observed resolution (48 keV) when the additional 25 keV inherent resolution is added in quadrature. A significant Fermi part of the decay would broaden these peaks (to about 62 keV FWHM for a pure Fermi transition).

3. *Pulse-height ratio selection*

The primary means of identifying ^{16}N α decays is the ratio of α to ^{12}C pulse heights for events detected in coincidence in opposing detectors. Figure 6 shows a two-dimensional spectrum (calibrated for α-particle energy) of the coincidence data for detector D4 versus D3. The intense diagonal bands of constant energy ratio are the α-^{12}C coincidences. The observed ratio is near 4:1 rather than the expected 3:1 (Sec. II A), since the energy calibration is not valid for the ^{12}C recoil nuclei due primarily to pulse-height defects in the detectors and greater energy losses in the collector foil and detector dead layer. The very small number of events outside these intense bands constitutes a measurement of the random background (except for low-energy β-β coincidences) and is seen to be negligible in the experiment.

In addition to the diagonal α-^{12}C bands, there are horizontal and vertical bands of events extending from the two main α-particle peaks down to very low energy. These are the tails of the response functions. Only the main α peak, due to the broad E_x = 9.59 MeV level of ^{16}O, is intense enough to exhibit a visible tail, but the tail contains almost as many counts as does the interference peak region. These degraded events can be clearly distinguished from the α particles in the region of the interference peak up to the beginning of the main peak.

[2]Weighted average of the values of Refs. [4,25].
[3]Deduced from Refs. [4,26].

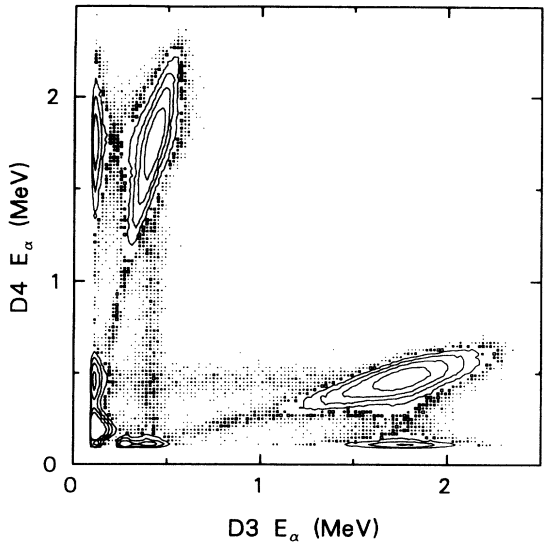

FIG. 6. Contour plot of coincident events recorded for detector D4 versus D3. The energy calibration is for α particles. Contour lines are shown for 30, 100, 300, and 1000 counts, and the minimum displayed intensity is one count.

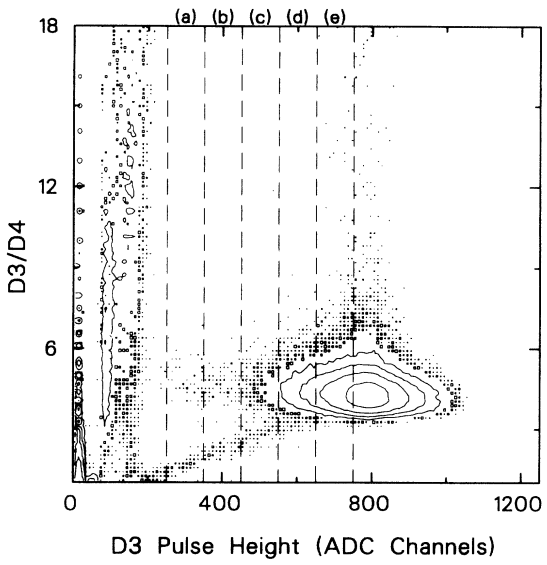

FIG. 7. Contour plot of the D3/D4 pulse-height ratio as a function of D3 pulse height. (a) to (e) denote regions used in Fig. 8. Contour lines are shown for 30, 100, 300, and 1000 counts, and the minimum displayed intensity is one count.

Because the degraded events are separate from the non-degraded events, a numerical subtraction is not required and hence the statistical accuracy of the data in the region of the secondary peak is not affected.

Finally, there are several features in Fig. 6 located near the axes that are due to β-α, β-^{12}C, and β-β coincidences. Because of the small β response of the thin detectors, these features are also separated from the α-^{12}C bands over the energy region of interest.

The available coincidence data were filtered using limits on the pulse-height ratio to retain only events in the diagonal α-^{12}C coincidence band. As an alternative representation, Fig. 7 shows a spectrum of pulse-height ratio (D3/D4) versus pulse height for detector D3, where the horizontal band of constant ratio (≈ 4) contains the acceptable events. Only ratios greater than unity are shown (e.g., an α particle in D3 and a ^{12}C recoil in D4). The tail of the α-particle response function appears here as a diagonal band leading from the main peak down towards the origin. The various particle-β coincidences, which tend to involve higher ratios, are clearly seen as vertical bands with a high D3/D4 ratio.

The two-dimensional ratio spectrum for each detector was divided into a series of α-particle energy bins, as shown in Fig. 7 for D3. The resulting one-dimensional ratio spectra, obtained by projection onto the D3/D4 axis, are given in Fig. 8. The peak corresponding to ^{16}O breakup is asymmetric with a well-defined low-ratio side (near D3/D4 = 3.0) and a tail on the high-ratio side due to the greater straggling of the ^{12}C particles. The degraded α-particle events can be seen as a peak at lower ratio [in Figs. 8(a)–8(c)], while the increasing numbers of counts at higher ratios are due to α-β coincidences. The low-ratio side of the α-^{12}C peak changes little with energy and its sharpness makes the choice of a low-ratio

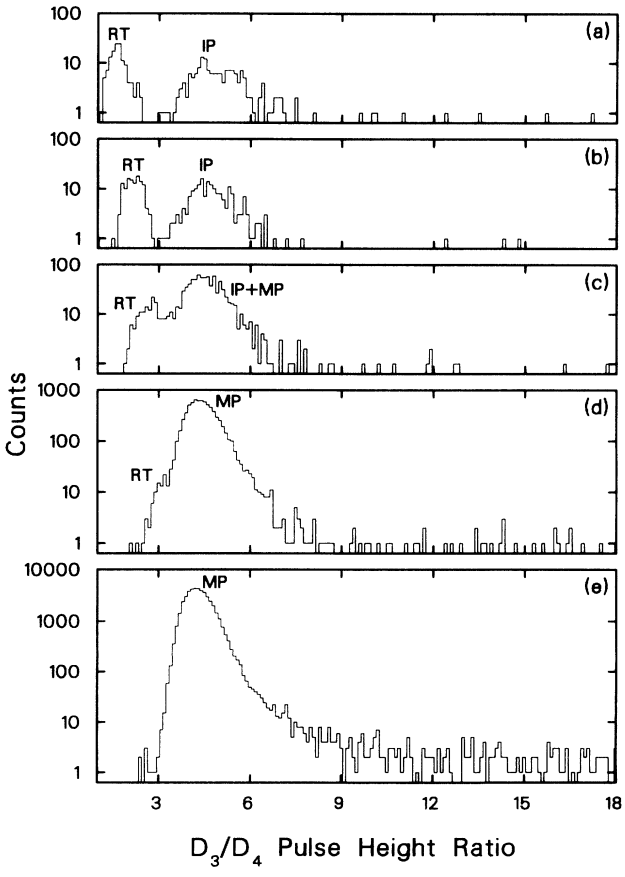

FIG. 8. Pulse-height-ratio spectra for different slices of Fig. 7. RT, IP, and MP indicate events due to the response tail, interference peak, and main peak, respectively.

limit for the analysis well defined. Although this ratio cut no longer completely excludes the degraded or tail events above about $E_\alpha = 1.1$ MeV, it does so far enough into the intense main peak that the contribution of the tail is relatively small and can be estimated from the strength at lower energies (see Fig. 10 in Sec. II D 5).

Choosing a high-ratio limit is not quite so straightforward. The α-^{12}C ratio peak has a high-ratio tail, while α-β random coincidences produce a peak at very high ratio which has a long, low-ratio tail. Also, the relative sizes and positions of these tails are energy dependent. However, as relatively few events are found in the region of uncertainty, the high-ratio limit is not required to be very precise and was set near 8, with the exact value detector dependent.

Figure 9 shows the effect of the ratio cut applied to the coincidence spectrum, summed over all detectors, which is compared with the spectrum of singles events. The relative intensity in the region of the interference peak is reduced by a factor of about two compared with the singles spectrum due to the exclusion of the degraded α particles, and the elimination of most ^{12}C and β events has exposed the interference region α peak to still lower energies. The constant background observed in the singles spectrum above 2.4 MeV is almost completely eliminated from the coincidence spectrum. The remaining high-energy events are attributed to the presence of ^{18}N (Sec. II D 4).

4. Subtraction of beam contaminants

Due to the molecular and multiply charged nature of the TISOL ion beam, small amounts of other radioactive species are present at the ^{16}N mass positions (see Sec. II A). The presence of possible proton or α-decaying contaminants would, in general, be detectable by their differing breakup energy ratios and they would be removed by the ratio cut. However, β-delayed α decays from isotopes with masses close to 16 are not separable from true ^{16}N decays and can contribute to the coincidence spectra. Two such contaminants were identified: ^{17}N and ^{18}N.

The presence of the 1.081 MeV α-particle peak from ^{18}N (from the ^{12}C^{18}N$^+$ molecule in the mass 30 beam) is clearly apparent in the spectra of Figs. 4 and 9. The high-energy tail of the broad 2.2 MeV ^{18}N peak can also be observed above 2.3 MeV. Because of its short half-life (0.62 s), little ^{18}N is present in detectors D3–D6. A normalized summed spectrum of D3 to D6 was subtracted from the summed D1+D2 spectrum, and the amount of contaminant present determined by matching the resultant spectrum to a known ^{18}N spectrum [27] in the region of 1.081 MeV. Corrections for the small amount of ^{18}N in D3 and D4, as well as the small amount of ^{17}N below 1.5 MeV (see below), were included in the calculation. A total of 630 ± 60 counts from ^{18}N was found in the ^{16}N spectrum (10^6 counts) and was subtracted.

A previously unreported β-delayed α-decay branch of ^{17}N ($t_{1/2} = 4.2$ s) was observed at mass 33 [27,28]. The total $\beta\alpha$-branching ratio was determined to be $(2.5 \pm 0.4) \times 10^{-5}$. Because most of the ^{17}N strength lies in the energy region of the main ^{16}N peak, and because of its longer half-life, it proved to be impossible to determine the amount of ^{17}N in the ^{16}N spectrum obtained from the mass 30 beam by the same method as used for ^{18}N. A γ-ray yield measurement indirectly determined the ratio of ^{17}N to ^{16}N in the mass 30 beam to be $(1.2 \pm 0.6) \times 10^{-3}$. This implies the presence of 2500 ± 1300 counts in the final coincidence spectrum due to ^{17}N events. Alternatively, K-matrix fits to the ^{16}N spectrum, including the region of the ^{17}N spectrum containing the narrow peak near

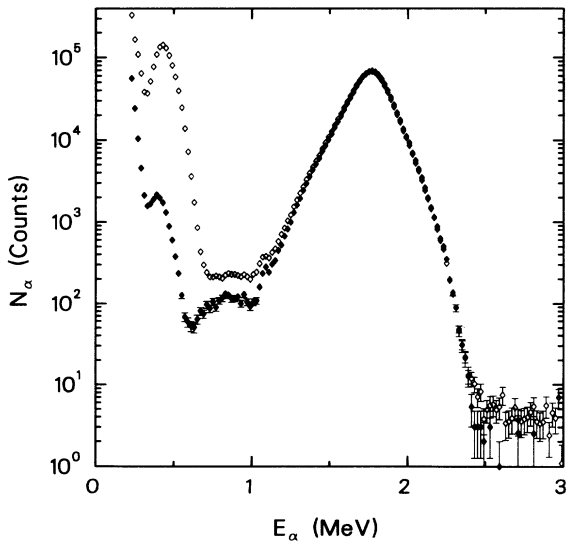

FIG. 9. Effect of the ratio requirement on the coincidence spectrum (solid diamonds) compared with the singles spectrum (open diamonds). The spectra have been summed over all detectors, and the summed spectra normalized to the same height.

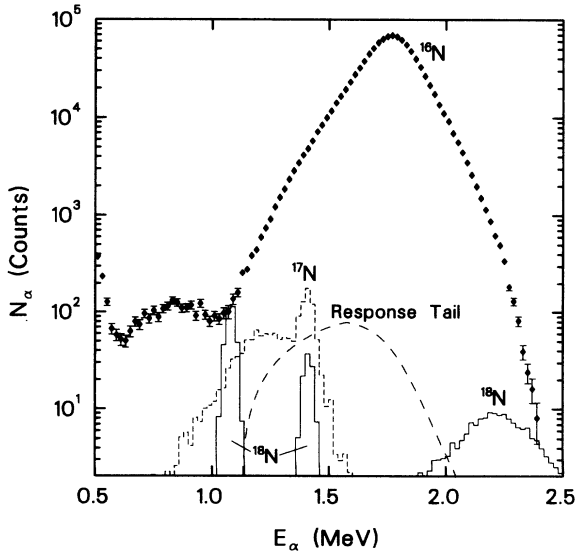

FIG. 10. Corrected coincidence spectrum showing the various contributions that have been subtracted. The contribution marked "response tail" does not include events already removed by the ratio cut.

1.4 MeV, and with the amount of ^{17}N to be subtracted treated as a free parameter, indicated the presence of approximately 1000 ± 600 counts with an additional uncertainty of at least ± 400 counts due to the exact form of the parametrization used. A value of 1500^{+2500}_{-1000} counts was chosen as a compromise between the two independent determinations. This amount of ^{17}N was subtracted and the uncertainty was included in the calculation of the systematic error (see Sec. III G). The ^{17}N and ^{18}N contributions that have been subtracted from the ^{16}N spectrum are shown in Fig. 10.

5. *Subtraction of the tail of the response function within the main peak*

As noted in Sec. II D 3, the tail of the response function in the region of the interference peak can be excluded by a suitable choice of the low-ratio limit. On the low-energy side of the main α peak, a correction is required for the unresolved portion of the tail (see Fig. 10). In the region of the interference peak, the magnitude of the tail of the response function was found to be a linear function, within statistics, of the α-particle energy; this property was used to extrapolate the contribution of the tail into the region of the main peak. Although the error associated with this estimate may increase with α-particle energy, the relative importance of the tail rapidly decreases with increasing energy as the total α-particle intensity increases so rapidly. A total of 1750 counts was subtracted. A variation of $\pm 100\%$ of this total produced a negligible effect on the value of $S_{E1}(300)$ (see Sec. III G).

6. *Coincidence efficiency*

An important concern is the dependence of the coincidence efficiency on energy, particularly in the interference-peak region, where the low-energy recoil ^{12}C ions have an increased chance of undergoing scattering. Calculations using the TRIM program [24] indicated no loss of efficiency over the full energy range of the experiment. In addition, experimental verification was possible. Following the ^{16}N runs, a high-count run for ^{18}N was performed with the same detector system (except for the replacement of D2 with a larger, thicker detector). A comparison of the singles to coincidence counts for the two lines, and for the broad peak, indicated that the coincidence efficiency as a function of energy was constant to within $\pm 1\%$ down to the energy of the lowest α peak at 1.081 MeV. Below this energy, the ^{16}N coincidence data, including the entire α-response tail, were compared with the singles events. Figure 11 shows the coincidence efficiency determined by this method. The efficiency, determined by a fit to the points in the interference-peak region, was found to be constant to within $\pm 6\%$ down to E_α=0.75 MeV. The apparent decrease in coincidence efficiency below this energy is due to the presence of the ^{12}C peak in the singles spectrum and consequent decrease in the ratio of coincidences to singles.

The coincidence efficiency was further investigated through the β-p decay of ^{17}Ne [29]. Each proton decay produces a corresponding ^{16}O recoil nucleus with 1/16 of the proton energy in the laboratory system, and thus provides an opportunity to verify the coincidence efficiency to very low ion energies (equivalent to $E_{^{12}C} \approx 200$ keV).

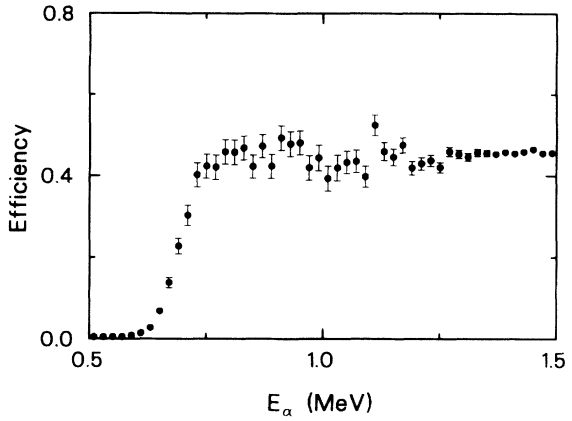

FIG. 11. Ratio of the number of coincidence events, including the response function tail, to the number of singles events as determined from the ^{16}N spectra. See Sec. II D 6 for an explanation of the decrease in ratio for $E_\alpha < 0.75$ MeV.

To observe the high-energy protons, a 500-μm-thick, silicon surface-barrier detector (D7) was mounted behind detector D1 (10.6 μm). An $A = 17$ beam was implanted into the collector foil for 0.3 s before target-wheel rotation. Because of its very short half-life (109 ms), only about 6% of the ^{17}Ne decay was detected. However, spectra of sufficient statistical accuracy were obtained without difficulty.

A complete proton singles spectrum in detector D7 was obtained, where the events for $E_p < 6.0$ MeV were also identified by a dE/dx versus E selection in D1 and D7. A corresponding proton-^{16}O coincidence spectrum (with ^{16}O detected in D2) was obtained and the appropriate pulse-height ratio cut applied. The coincidence efficiency

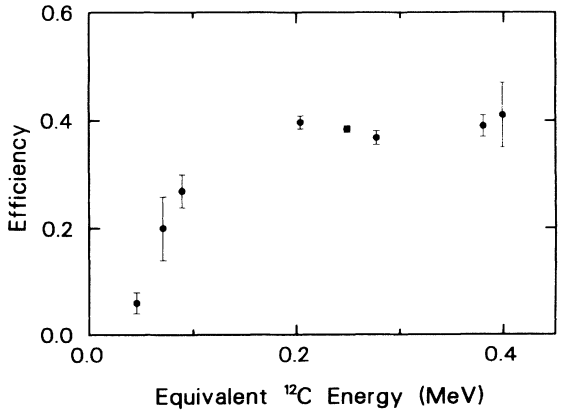

FIG. 12. The energy dependence of the coincidence detection efficiency for proton groups in the decay of ^{17}Ne, scaled for ^{12}C nuclei with the same velocity as ^{16}O nuclei from ^{17}Ne decay.

was determined by calculating the ratio of coincidence to proton singles, and is plotted in Fig. 12 for the monoenergetic proton groups. The coincidence efficiency for ^{16}O events should be the same as for ^{12}C with the same velocity. The curve in Fig. 12 implies that the coincidence efficiency for detecting α-^{12}C pairs is constant down to $E_\alpha \approx 550$ keV.

7. Background events and the low-energy cutoff

The energy down to which the α-^{12}C coincidence spectra are free from background is determined by the rapid increase of ^{12}C-β coincidences below about E_α = 600 keV. To investigate the form of the ^{12}C-β coincidence spectrum in the interference region and to determine the low-energy cutoff for the α-^{12}C data, the ratio-cut analysis described in Sec. II D 3 was repeated with "nonphysical" detector pairs (e.g., D1 versus D5) so that no true coincidences were in the resulting spectra [30]. The number of events observed in this manner represents the random rate to be expected in the measurement. The results showed that the random rate was negligible.

In addition to low-energy ^{12}C-β events, a few coincidences were observed at higher energies. Several of these events were attributed to random α-^{12}C coincidences, but most appeared to be due to electrical noise that affected only two detectors. Some of these events occurred in the region of the ^{16}N interference peak. From the number of these noise events, it is estimated that less than 1 noise count per 20 keV bin is present in the final summed-coincidence spectrum.

From the observed sharp increase of ^{12}C-β events with decreasing energy, low-energy cutoffs were chosen for each individual detector-coincidence spectrum. The lowest cutoff was E_α = 580 keV for D2 and D3, and the highest was E_α = 650 keV for D6 with the others ranging in between. The four lowest-energy points in the coincidence spectrum have been corrected for loss of events in detectors D1, D4, D5, and D6 by normalizing to the low-energy, low cutoff spectra of detectors D2 and D3 (see Fig. 13). The additional uncertainty due to this normalization has been included in the errors assigned to these data points.

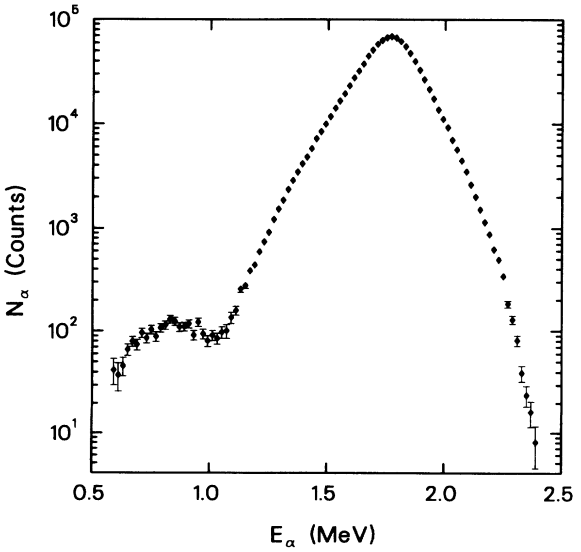

FIG. 13. The final corrected and summed coincidence spectrum. The spectrum contains 1.0265×10^6 counts.

E. Final spectra

All corrections and cuts described in the preceding sections have been applied individually to produce the

TABLE I. The final corrected and summed coincidence data. All entries have been rounded to the nearest integer. Fits described in Sec. III were made to the unrounded data. The total number of counts is 1.0265×10^6.

E_α keV	N counts	Δ counts	E_α keV	N counts	Δ counts
590	42	12	1510	11699	109
610	37	11	1530	14123	119
630	46	9	1550	16479	129
650	66	8	1570	19328	139
670	79	9	1590	23139	152
690	74	9	1610	27525	166
710	96	10	1630	32084	179
730	85	9	1650	37498	194
750	103	10	1670	44569	211
770	88	9	1690	50869	226
790	107	10	1710	58048	241
810	115	11	1730	63084	251
830	131	12	1750	67052	259
850	125	11	1770	68715	262
870	109	11	1790	66582	258
890	110	11	1810	61700	249
910	117	11	1830	55137	235
930	91	10	1850	47419	218
950	122	11	1870	39660	199
970	94	10	1890	32748	181
990	80	10	1910	26568	163
1010	91	10	1930	21314	146
1030	85	11	1950	17317	132
1050	97	13	1970	13556	117
1070	100	15	1990	11037	105
1090	135	17	2010	9189	96
1110	159	16	2030	6956	83
1130	256	18	2050	5626	75
1150	277	18	2070	4414	67
1170	384	21	2090	3460	59
1190	439	23	2110	2602	51
1210	590	26	2130	1976	45
1230	736	29	2150	1501	39
1250	908	32	2170	1137	34
1270	1212	36	2190	868	30
1290	1520	40	2210	617	25
1310	1848	44	2230	491	22
1330	2331	49	2250	339	19
1350	2854	54	2270	183	14
1370	3430	60	2290	129	12
1390	4128	66	2310	81	9
1410	4800	71	2330	39	7
1430	5758	77	2350	24	6
1450	7162	85	2370	16	5
1470	8417	92	2390	8	4
1490	9959	100			

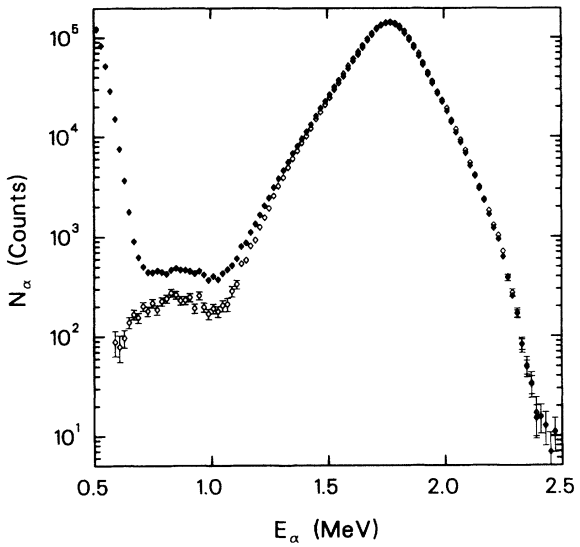

FIG. 14. Final summed singles spectrum (solid diamonds) and coincidence spectrum (open diamonds) normalized to the singles spectrum at the main α-particle peak.

summed-coincidence spectrum given in Fig. 13 and listed in Table I. Mainly because of an improved energy calibration, there are small differences between the spectrum shown in Fig. 13 and that in Ref. [19].

A final summed-singles spectrum was also obtained with all the corrections described in previous sections that are applicable to singles detection (see Fig. 14). There are 2.2×10^6 events in the spectrum. Also shown in Fig. 14 is the coincidence spectrum normalized to the singles spectrum at the peak.

1. Comparison with the data of Ref. [14]

A previous measurement of the β-delayed α-particle spectrum of ^{16}N of high statistical accuracy has been reported [14]. This singles spectrum was obtained using 35 μm detectors. However, no tabulated version of this spectrum has been published. The spectrum used in the fits of Refs. [13,17,18,31,32] is a subset of the data of Ref. [14] resulting from a private communication [33] to one of the authors. This spectrum contains only every fourth data point and the error bars have been enlarged to include systematic errors from the energy calibration.

The complete data set of Ref. [33] is shown in Fig. 15 where it is normalized to the present coincidence spectrum. The data of Ref. [33] are the result of a "singles" spectrum for which no corrections have been made for the response function of the system.

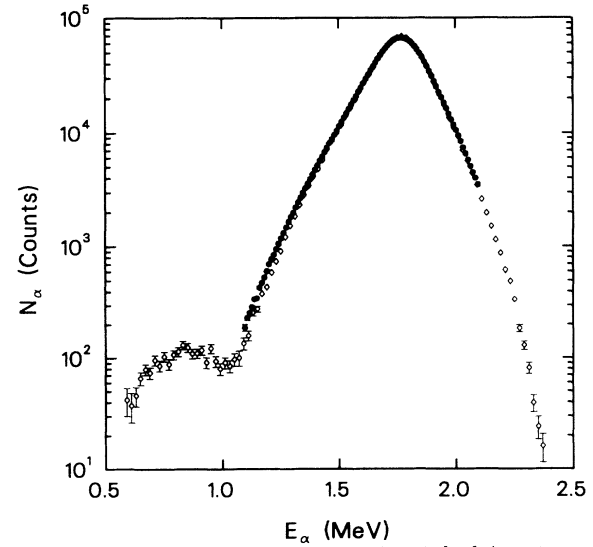

FIG. 15. The complete spectrum of Ref. [33] (solid circles) normalized to the present coincidence spectrum (open diamonds).

III. THEORETICAL FITS

A. Introduction

The β-delayed α spectrum of ^{16}N, and the ^{12}C + α elastic-scattering phase shifts, have been employed in several analyses [13,17,18,31,32,34] in attempts to improve the reliability and precision of the extrapolation of the $E1$ radiative capture cross section down to the astrophysically interesting region at E = 300 keV; both R- and K-matrix formulations have been used to provide the theoretical basis for the extrapolation. This approach permits the simultaneous fitting of a theoretical model to the three kinds of experimental data. With the extended range and precision of the present α spectrum, a much more reliable and precise extrapolation can now be achieved.

The general philosophy behind both R- and K-matrix approaches is that contributions to each of the processes discussed above can be parametrized in terms of the properties of a few nearby states. The remaining states are farther away in energy and therefore do not induce any rapid variations over the region of interest. As a result, they may be represented by smooth background terms. There are, however, many different ways to account for the nearby states and to treat the background terms. In addition to the well-known differences between the R- and K-matrix approximations to the full scattering matrix, there are also several variants within each method. Unfortunately, different methods of parametrization usually lead to somewhat different final values for the extrapolated S factor. Since the parameters in the various approaches are not necessarily independent of one another, the effect on the extrapolation due to individual parameters cannot be easily isolated; this has led to many discussions [13,31,32]. It is not our purpose here to enter into a debate on what constitutes the optimum model—our interest is limited to extracting the best possible value for the S factor using, as far as possible, the standard approaches already in the literature.

In this section simultaneous fits to the β-delayed α spectrum of ^{16}N and to existing α scattering and radiative capture data sets, using both R- and K-matrix parametrizations, will be described and limits placed on the value of $S_{E1}(300)$, the $E1$ part of the astrophysical S factor for the ^{12}C$(\alpha,\gamma)^{16}$O reaction at a most effec-

tive energy of 300 keV. The initial approach is that of Refs. [13,31,32] for the R matrix and of Ref. [18] for the K matrix. The previous approaches will be modified or extended where appropriate. Each analysis will be considered separately and the results compared in Sec. IV.

B. General use of the data

The measured ^{16}N β-delayed α spectrum covers the center-of-mass energy range of $0.787 \leq E \leq 3.190$ MeV (bin central energy). Due to a small contribution from the narrow 2^+ state at $E_x = 9.84$ MeV ($E = 2.68$ MeV) the four points between $E = 2.64$ and 2.75 MeV have been excluded from the fitting, leaving 87 data points ($N_\beta = 87$), each with a bin width of 26.7 keV.

Measurements of the ^{12}C$(\alpha,\gamma)^{16}$O radiative capture cross section have been reported in Refs. [5–11]. Of these, only Refs. [7,9–11] report results for which $\sigma_{E1}(\alpha,\gamma)$ has been separated from the total cross section, and only these are included in the fits to the present work. These cover the range $0.94 \leq E \leq 2.98$ MeV ($N_\gamma = 71$). Fits to the combined data set are made as well as to the separate data sets (Secs. III E 1, III E 2, and III J). Because of the large systematic differences in the cross section measurements, the final S factor is based on the analysis with the combined data set.

Values of $\ell = 1$ and $\ell = 3$ phase shifts were taken from Plaga *et al.* [35] for $E_\alpha \leq 6.56$ MeV ($E \leq 4.92$ MeV). In our fits, we omit their values at $E_\alpha = 3.571$ MeV ($E = 2.678$ MeV), as has been done in Refs. [17,18,34], since the $\ell = 1$ phase shift at this energy differs from the fitted value by over six times the assigned error. This discrepancy could be due to incomplete separation of the scattering anomaly due to the narrow 2^+ level. Also, values of the $\ell = 1$ phase shift for $E_\alpha > 5.05$ MeV ($E > 3.79$ MeV) are omitted because they show an irregular energy dependence, and because there is a 1^- level at $E_x = 12.44$ MeV ($E = 5.28$ MeV) that we do not wish to include explicitly. If it were included, then a further 1^- level at $E_x = 13.09$ MeV should also be included, because these two levels are strongly isospin mixed. Thus the $\ell = 1$ phase shift is fitted for $E \leq 3.79$ MeV ($N_{\delta 1} = 26$) and the $\ell = 3$ phase shift for $E \leq 4.92$ MeV ($N_{\delta 3} = 40$). Two other α-scattering phase-shift data sets [36,37] have been incorporated into previous analyses. However, since the energy scales of both data sets have been recalibrated [13], and because the Jones data [36] do not have quoted uncertainties, both sets were excluded from the present analysis.

The $\ell = 3$ phase shift data are included in all the fits. These data are of little significance in the K-matrix calculation (as was also found in Ref. [34]) but were retained in the analysis to allow a more direct comparison with the R-matrix analysis for which they place additional restrictions on fits at extreme values of the channel radius a.

The energy and γ width of the 1^- level at $E_x = 7.117$ MeV ($E = -0.045$ MeV) and the energy of the 3^- level at $E_x = 6.130$ MeV ($E = -1.032$ MeV) were taken from Ref. [4]. The β-feeding amplitudes to these levels were determined from the known branching ratios [4].

C. General fitting procedures

As in any nonlinear least-squares calculation, we started with an initial estimate of the parameters. With this set, the α-particle spectrum of ^{16}N, the ^{12}C$(\alpha,\gamma)^{16}$O cross section, and the ^{12}C + α phase shifts were calculated. To fold in the effect of finite-energy resolution on the α-particle data, the calculated spectrum was convoluted with an energy-independent Gaussian resolution function corresponding to 30 keV FWHM (see Sec. II D 2) in the laboratory.

The fitting parameters were adjusted to minimize the quantity

$$\chi^2 = \sum_r \chi_r^2 = \chi_\beta^2 + \chi_{\delta 1}^2 + \chi_{\delta 3}^2 + \chi_\gamma^2, \tag{1}$$

where $r = \beta, \delta 1, \delta 3, \gamma$ for the ^{16}N β decay, the $\ell = 1$ and 3 phase shifts, and the ^{12}C$(\alpha,\gamma)^{16}$O data, respectively. Here

$$\chi_r^2 = \sum_{k=1}^{N_r} \left(\frac{Y_r^{\rm expt}(E_k) - Y_r^{\rm calc}(E_k)}{\delta Y_r(E_k)} \right)^2, \tag{2}$$

where $Y_r^{\rm expt}$ is the experimental value, $Y_r^{\rm calc}$ the calculated value, δY_r the experimental error, and N_r the number of data points for each particular reaction. The convoluted α-particle spectrum was used for $Y_r^{\rm calc}(E_k)$ in the case of ^{16}N β decay. The value of χ^2 was minimized using the computer routine MINUIT [38] yielding the final value $\chi^2_{\rm min}$ and a final set of parameters.

From the best-fit parameter values, the ^{12}C$(\alpha,\gamma)^{16}$O $E1$ cross section σ_{E1} was calculated at the energy of astrophysical interest ($E = 300$ keV) and the corresponding S factor $S_{E1}(300)$ obtained from the relation

$$S_{E1} = E e^{2\pi\eta} \sigma_{E1}, \tag{3}$$

where $\eta = Z_1 Z_2 e^2/\hbar v$ is the Sommerfeld parameter.

If all the experimental uncertainties followed Gaussian distributions and δY_r were the standard deviations, then a 1σ uncertainty in a particular parameter could be taken as the change in the value of that parameter that increases $\chi^2_{\rm min}$ by unity. For this to be valid, one expects $\chi^2_{\rm min} \approx \nu = \sum_r N_r - N_p$, where ν is the number of degrees of freedom and N_p is the number of parameters to be varied. The $\chi^2_{\rm min}$ found is actually 1.8 times this value. This is caused mainly by the systematic differences between the different ^{12}C$(\alpha,\gamma)^{16}$O data sets [see Fig. 19(b)]. Subjectively, we take acceptable fits to be those for which $\chi^2 \leq \chi^2_{\rm min}(1 + 9/\nu)$, which is similar to the 1σ estimate used in Ref. [34].

Systematic errors were derived by varying the quantity under investigation within a reasonable range about its best-fit value. These errors are discussed in the context of the particular parametrization in Sec. III G. Systematic errors introduced by the substantial differences in the four radiative α-capture data sets are discussed further in Sec. III J.

D. Formalism

For convenience in comparing with the existing literature, we shall follow closely the notation generally used in R- and K-matrix calculations. The central equations are summarized below mainly to define the notation. In particular, we point out one difference in notation. Each level energy requires two labels: ℓ indicating the orbital angular momentum (equal to J here) and λ indicating the level number. In the R matrix the energy is usually represented by $E_{\lambda\ell}$. However, in the K matrix it is usually given as $E_{\ell\lambda}$. Thus E_{13} in the R matrix means the energy of the first f-wave state, while in the K matrix it means the energy of the third p-wave state.

The general expressions given in the next two sections provide the basis for a search for the appropriate set of parameters. The final results, for the most part, are obtained using three 1^- levels and three 3^- levels, with additional constant background terms in the K-matrix formalism. The first two 1^- levels are the subthreshold $E_x = 7.117$ MeV level and the broad $E_x = 9.59$ MeV level, while the third is a background level lying above the energy range being fitted. Similarly, the 3^- levels are the subthreshold $E_x = 6.130$ MeV level, the broad $E_x = 11.6$ MeV level, and a higher-lying background level.

1. *R-matrix formalism*

The R-matrix formulas to fit the data under discussion are taken from [13] and are summarized here for convenience.

For the β-delayed α spectrum following the decay of ^{16}N, the number of α-particles per unit energy is given by the expression

$$W_\alpha(E) = f_\beta(E) \sum_{\ell=1,3} P_\ell(E,a_\ell) \left| \frac{\sum_{\lambda=1}^{q_\ell} \frac{A_{\lambda\ell}}{E_{\lambda\ell}-E}}{1-[S_\ell(E,a_\ell)-B_\ell+iP_\ell(E,a_\ell)]R_\ell(E)} \right|^2 , \tag{4}$$

where $f_\beta(E)$ is the integrated Fermi function (determined from an extended-nucleus expression [39]), $P_\ell(E,a_\ell)$ and $S_\ell(E,a_\ell)$ are the penetration factor and shift factor calculated at the channel radius a_ℓ [40], and B_ℓ is the constant boundary parameter. Also, the function $R_\ell(E)$ is

$$R_\ell(E) = \sum_{\lambda=1}^{q_\ell} \frac{\gamma_{\lambda\ell}^2}{E_{\lambda\ell}-E} . \tag{5}$$

The sums extend over q_ℓ levels, specified by their eigenenergies $E_{\lambda\ell}$ and α-particle reduced width amplitudes $\gamma_{\lambda\ell}$. The $A_{\lambda\ell}$ in Eq. (4) are energy-independent β-feeding amplitudes.

The $E1$ part of the ^{12}C$(\alpha,\gamma)^{16}$O cross section is given by

$$\sigma_{E1}(E) = \frac{6\pi}{k_\alpha^2} P_1 \left| \frac{\sum_{\lambda=1}^{q_1} \frac{\gamma_{\lambda 1}\Gamma_{\lambda\gamma}^{1/2}}{E_{\lambda 1}-E}}{1-(S_1-B_1+iP_1)R_1} \right|^2 , \tag{6}$$

where k_α is the α-particle wave number and $\Gamma_{\lambda\gamma}(E)$ is the formal $E1$ γ-ray width of the level λ;

$$\Gamma_{\lambda\gamma} = 2E_\gamma^3 \gamma_{\lambda\gamma}^2, \tag{7}$$

with constant $\gamma_{\lambda\gamma}$.

The ^{12}C+α elastic-scattering phase shift is given by

$$\delta_\ell(E) = -\Phi_\ell + \arctan\left[\frac{P_\ell}{R_\ell^{-1}-S_\ell+B_\ell}\right], \tag{8}$$

where $-\Phi_\ell$ is the hard-sphere phase shift calculated at a_ℓ [40].

It has been shown [44] that identical fits to the data can be obtained for any choice of the B_ℓ value, provided that the level parameters are adjusted suitably. It is simplest to make use of the information regarding the subthreshold levels by choosing $B_\ell = S_\ell(E_{1\ell})$. Then, $E_{1\ell}$ is equal to the observed energy of the level, and one also has

$$A_{1\ell}^2 = \frac{N_\alpha Y_{1\ell}}{Y(9.59) I_{1\ell} f_{1\ell}} \tag{9}$$

with

$$I_{1\ell} = \pi\gamma_{1\ell}^{-2} \left(1+\gamma_{1\ell}^2 \frac{dS_\ell}{dE}\right)_{E_{1\ell}}^{-1} , \tag{10}$$

and $\Gamma_{1\gamma}^{\rm obs}$, the observed γ width, is

$$\Gamma_{1\gamma}^{\rm obs} = \Gamma_{1\gamma} \left(1+\gamma_{11}^2 \frac{dS_1}{dE}\right)_{E_{11}}^{-1} . \tag{11}$$

Here N_α is the total number of counts in the α spectrum, $Y_{1\ell}$/Y(9.59) is the branching ratio to the subthreshold level relative to that of the $E_x = 9.59$ MeV level in ^{16}O, and $f_{1\ell} = f_\beta(E_{1\ell})$. It is the observed width $\Gamma_{1\gamma}^{\rm obs}$ that is identified with the measured half-width of 55 meV [4] of the $E_x = 7.117$ MeV level, so determining the value of $\gamma_{1\gamma}$ (for given γ_{11}). There are then 17 adjustable parameters, including the channel radius a (we assume $a_1 = a_3 = a$). In the following all parameter values are for $B_\ell = S_\ell(E_{1\ell})$, unless otherwise stated.

In addition to these fits with $B_1 = S_1(E_{11})$, we have also carried out fits with $B_1 = S_1(300\ \text{keV})$, as in Ref. [17], in order to use the S factor at 300 keV rather than γ_{11} as one of the fitting parameters. The fitted values for both approaches were routinely converted to each other [44] and excellent agreement was found.

2. *K-matrix formalism*

A K-matrix analysis for the $E1$ part of the $^{12}C(\alpha,\gamma)^{16}O$ cross section and the $^{12}C(\alpha,\alpha)^{12}C$ $\ell = 1$ phase shift was developed in Refs. [41,42] and was extended to include the β-delayed α-particle spectrum of ^{16}N in Refs. [18,34]. The notation used here most closely follows that of Refs. [18,42]. The α spectrum from the decay of ^{16}N is written as

$$W_\alpha(E) = f_\beta(E) \sum_{\ell=1,3} p^2_{\ell\alpha}(E) \times \frac{\left|\sum_{\lambda=1}^{q_\ell} \frac{B_{\ell\lambda}\, g_{\ell\alpha\lambda}}{E_{\ell\lambda}-E} + D_{\ell\beta\alpha}(E)\right|^2}{1+p^4_{\ell\alpha}(E)K^2_{\ell\alpha\alpha}(E)}. \quad (12)$$

The $E1$ part of the $^{12}C(\alpha,\gamma)^{16}O$ cross section takes on the form

$$\sigma_{E1}(E) = \frac{12\pi}{k^2_\alpha} p^2_{1\alpha} p^2_{1\gamma} \frac{\left|\sum_{\lambda=1}^{q_1} \frac{g_{1\gamma\lambda}\, g_{1\alpha\lambda}}{E_{1\lambda}-E} + D_{1\gamma\alpha}\right|^2}{1+p^4_{1\alpha}K^2_{1\alpha\alpha}}. \quad (13)$$

The elastic-scattering phase shift is given by

$$\delta_\ell(E) = \arctan(p^2_{\ell\alpha}K_{\ell\alpha\alpha}) \quad (14)$$

with

$$K_{\ell\alpha\alpha} = \sum_{\lambda=1}^{q_\ell} \frac{g^2_{\ell\alpha\lambda}}{E_{\ell\lambda}-E} + D_{\ell\alpha\alpha}. \quad (15)$$

Here, $p^2_{\ell c}(E)$ is the K-matrix penetrability for channel c ($c = \alpha, \gamma$) [42], $E_{\ell\lambda}$ is the level energy, $g_{\ell c\lambda}$ is the reduced width amplitude for channel c, and $B_{\ell\lambda}$ is the β-feeding amplitude. The energy-dependent background terms are

$$D_{\ell\alpha\alpha} = \frac{g^2_{\ell\alpha 3}}{E_{\ell 3}-E} + b_{\ell\alpha\alpha}, \quad D_{\ell\beta\alpha} = \frac{B_{\ell 3}\, g_{\ell\alpha 3}}{E_{\ell 3}-E} + b_{\ell\beta\alpha},$$

$$D_{1\gamma\alpha} = \frac{g_{1\gamma 3}\, g_{1\alpha 3}}{E_{13}-E} + b_{1\gamma\alpha}. \quad (16)$$

Note that in Refs. [18,34] $b_{1\beta\alpha}$ was not used. In previous work E_{13} was usually set a few MeV above the energy range of interest and was fixed, for example, at 8 MeV in Ref. [34]. However, we have allowed E_{13} to vary freely in the fit to any energy greater than E_{12} (see Sec. III H). Because of the possible presence of echo poles (pole terms with imaginary reduced width amplitudes and β-decay feeding amplitudes [18,43]), we allow $g^2_{\ell\alpha 3}$ to take on negative values.

As in Ref. [18], we fix three of the four parameters of the subthreshold resonance [the state energy (E_{11}), gamma-reduced width amplitudes ($g_{1\gamma 1}$), and β-decay feeding amplitude (B_{11})] from previous measurements of the properties of this level and the relative ^{16}N branching ratios [4]. Hence, there are 12 free $\ell = 1$ parameters: $g_{1\alpha 1}$, the four parameters for each of the $E_x = 9.59$ MeV and background levels, and the three background constants.

As was the case for the p wave, E_{31} and B_{31} for the subthreshold level were determined from external measurements. In order to reduce the number of f-wave parameters, we take $B_{33} = 0$; then E_{33} appears only in the $\ell = 3$ elastic-scattering analysis where its variation has little effect and it was set arbitrarily at $E_{33} = 15$ MeV. Thus, there are 7 free $\ell = 3$ parameters.

E. Results

1. *R-matrix fits*

The general R-matrix formulation as outlined in Sec. III D 1 contains more adjustable parameters than can be reasonably determined from fitting the available experimental data. In some earlier work [13,31,32], arguments based on isospin mixing or other models were used to limit the values of the amplitude $\gamma_{3\gamma}$ as well as the feeding amplitudes $A_{3\ell}$ to, and the energies $E_{3\ell}$ of, the background states for both $\ell = 1$ and 3. With the addition of the present experimental information, some of the restrictions may be relaxed. Our results show that the constraints on the p-wave feeding amplitudes cannot easily be sustained. At the same time, the fits are improved if the energies of the background states are allowed to vary.

For the f-wave analysis of the α spectrum, the initial analysis included the three states listed in Sec. III D. However, it was found that the minimum of χ^2 occurs in the region near $A_{23} = A_{33} = 0$ and, by taking $A_{23} = A_{33} = 0$, the value of $\chi^2_{\min}$ was increased by less than 1. The extrapolated value of the S factor was changed by 1 keV b, and the acceptable range of $S_{E1}(300)$ was narrowed only slightly from ± 19 to ± 16 keV b. We have therefore decided to take $A_{23} = A_{33} = 0$, thereby reducing the number of free f-wave parameters by two.

We recall that the R-matrix analysis for the f wave is performed with the boundary condition $B_3 = S_3(E_{13})$ [44]. The values $A_{23} = A_{33} = 0$ must therefore be transformed to their "physical" values for which $B_3 = S_3(E_{23})$ and $S_3(E_{33})$, respectively. Upon such a transformation the physical values of A_{23}/γ_{23} and A_{33}/γ_{33} are found to be indeed small compared with A_{13}/γ_{13}, and thus the assumption that $A_{23} = A_{33} = 0$ at $B_3 = S_3(E_{13})$ is consistent with the previous shell-model arguments [13].

Next we investigate the best value of the channel radius parameter a. Figure 16 shows the dependence of the total χ^2 on $S_{E1}(300)$ and a for $A_{23} = A_{33} = 0$. The minimum occurs at $a = 6.5$ fm and $S_{E1}(300) = 78.7$ keV b with a $\chi^2_{\min}$ of 376.9. Values of $\chi^2_{\min}$, as well as its components, are plotted as functions of channel radius a in Fig. 17(a), and the corresponding values of $S_{E1}(300)$ are plotted in Fig. 17(b). Table II shows the dependence of the values of the R-matrix parameters on a. We note that, for large a, $S_{E1}(300)$ decreases with increasing a as shown in Fig. 17(b). Figure 18 shows χ^2, and its components, as functions of $S_{E1}(300)$ determined along a cut through the contour plot of Fig. 16 at the best channel radius of $a = 6.5$ fm. The best fits to the experimental data for $a = 6.5$ fm are shown in Figs.

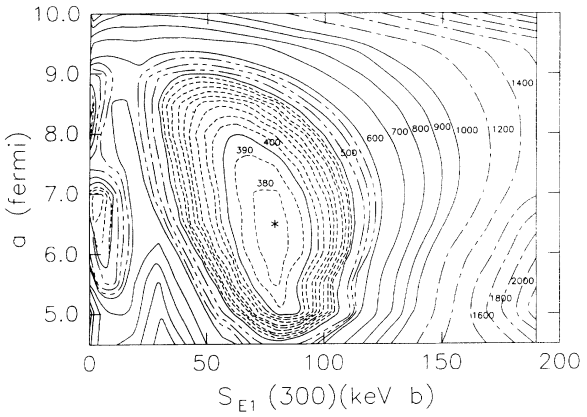

FIG. 16. Contour plot of $\chi^2[a, S_{E1}(300)]$ for $A_{23} = A_{33} = 0$. Long-dashed lines indicate steps of 10 in χ^2, short-dashed lines indicate steps of 25, full lines indicate steps of 100, and bold dash-dot lines indicate steps of 200. The best-fit value is indicated by the asterisk.

19(a)–(d). Table III, column 1, gives the values of the parameters and other quantities for the overall best fit with $B_\ell = S_\ell(E_{1\ell})$. In column 2, parameter values for each level λ are for $B_\ell = S_\ell(E_{\lambda\ell})$ [13].

For the reasons stated above, the value of $S_{E1}(300)$ and its possible range are derived from the calculations for the case of the f-wave β-feeding amplitudes $A_{23} = A_{33} = 0$. The fit criterion given in Sec. III C yields $\chi^2 \leq 376.9 + 9(1.8) = 393$. From the contour plot in Fig. 16, acceptable fits are obtained for values of a from 5.0 to 7.7 fm, and for $S_{E1}(300)$ from 63 to 95 keV b. Therefore, we take $S_{E1}(300) = 79 \pm 16$ keV b.

The values of the reduced α-particle widths are given in the last column of Table III for the best-fit radius of $a = 6.5$ fm. In R-matrix fits, these values depend sensitively on the channel radius. Values obtained with different channel radii cannot usefully be compared (most published values are for a around 5.5 fm). The same applies, though not quite so strongly, to the dimensionless reduced widths [13], θ^2_α, where values for the two dominant $\ell = 1$ states are $\theta^2_{\alpha,11}(7.12) = 0.013$ and $\theta^2_{\alpha,21}(9.60) = 0.45$ for $a = 6.5$ fm.

TABLE II. Parameter values for the best R-matrix fit for different channel radii a with $A_{23} = A_{33} = 0$. The boundary condition $B_\ell = S_\ell(E_{1\ell})$, the shift functions at the subthreshold states. Quantities in parentheses denote fixed input values; those in brackets are calculated from a fixed input plus one fitted parameter ($\gamma_{1\ell}$).

a (fm)	5.0	6.0	7.0
E_{11} (MeV)	(−0.0451)	(−0.0451)	(−0.0451)
γ_{11} (MeV$^{1/2}$)	0.269	0.117	0.0540
$\gamma_{1\gamma}$ (MeV^{-1})	[8.921×10^{-6}]	[8.778×10^{-6}]	[8.747×10^{-6}]
$A_{11}/\sqrt{N_\alpha}$(MeV$^{1/2}$)[a]	[0.329]	[0.141]	[0.064]
E_{21} (MeV)	3.830	3.028	2.728
γ_{21} (MeV$^{1/2}$)	0.675	0.417	0.270
$\gamma_{2\gamma}$ (MeV^{-1})	-5.858×10^{-7}	-2.033×10^{-6}	-2.566×10^{-6}
$A_{21}/\sqrt{N_\alpha}$ (MeV$^{1/2}$)[a]	0.309	0.0676	0.1369
E_{31} (MeV)	22.98	12.52	10.30
γ_{31} (MeV$^{1/2}$)	2.138	1.085	0.933
$\gamma_{3\gamma}$ (MeV^{-1})	-7.828×10^{-6}	-3.859×10^{-6}	-1.930×10^{-6}
$A_{31}/\sqrt{N_\alpha}$ (MeV$^{1/2}$)[a]	−0.648	−0.726	−0.523
E_{13} (MeV)	(−1.032)	(−1.032)	(−1.032)
γ_{13} (MeV$^{1/2}$)	0.219	0.107	0.0558
$A_{13}/\sqrt{N_\alpha}$ (MeV$^{1/2}$)[a]	[0.549]	[0.269]	[0.138]
E_{23} (MeV)	5.421	5.000	4.647
γ_{23} (MeV$^{1/2}$)	0.319	0.299	0.216
$A_{23}/\sqrt{N_\alpha}$ (MeV$^{1/2}$)[a]	0	0	0
E_{33} (MeV)	109.6	27.9	15.92
γ_{33} (MeV$^{1/2}$)	5.051	1.720	1.126
$A_{33}/\sqrt{N_\alpha}$ (MeV$^{1/2}$)[a]	0	0	0
$S_{E1}(300)$ (keV b)	85[b]	81[b]	75[b]
χ^2_β ($N = 87$)	100	99	102
$\chi^2_{\delta 1}$ ($N = 26$)	34.5	33.3	34.0
$\chi^2_{\delta 3}$ ($N = 40$)	62.8	59.9	59.5
χ^2_γ ($N = 71$)	189	186	183
$\chi^2_{\min}$ ($N = 224$)	386	377	379

[a]Division by $\sqrt{N_\alpha} = (1.0265\times10^6)^{1/2}$ removes the dependence of the values of these parameters on the number of α counts collected.

[b]Nonfinal values quoted for comparison purposes only.

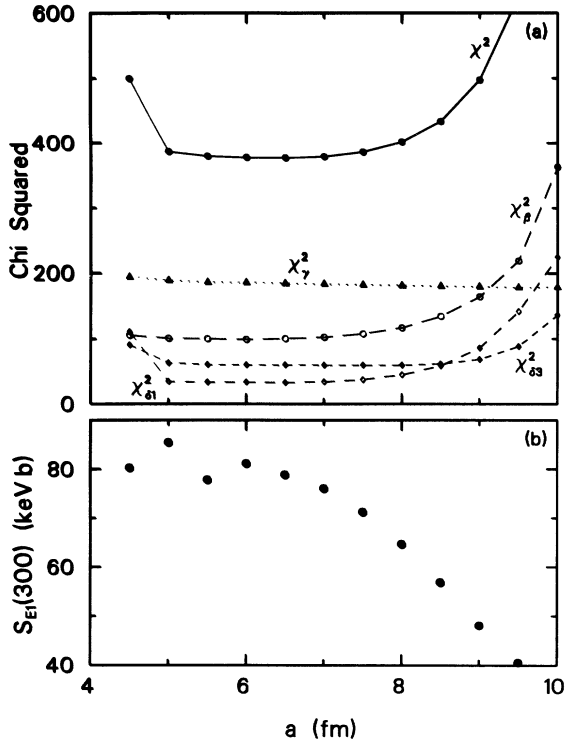

FIG. 17. (a) Minimum values of χ^2 and its components as functions of the channel radius a for $A_{23} = A_{33} = 0$. (b) Corresponding values of $S_{E1}(300)$. The lines connecting the points are simply guides to the eye.

2. *K-matrix fits*

As with the R matrix, the K-matrix parametrization outlined in Sec. III D 2 involves more adjustable parameters than can reasonably be determined from the data. We first examine the effect of the f-wave back-

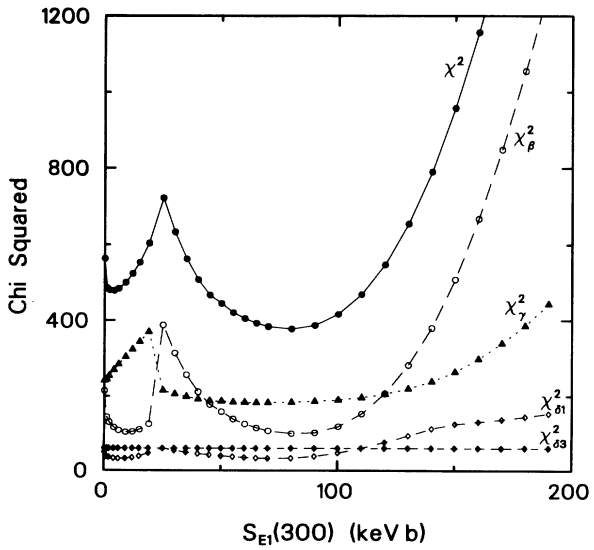

FIG. 18. Variation of χ^2 and its components along a cut through Fig. 16 at $a = 6.5$ fm. The lines connecting the points are simply guides to the eye.

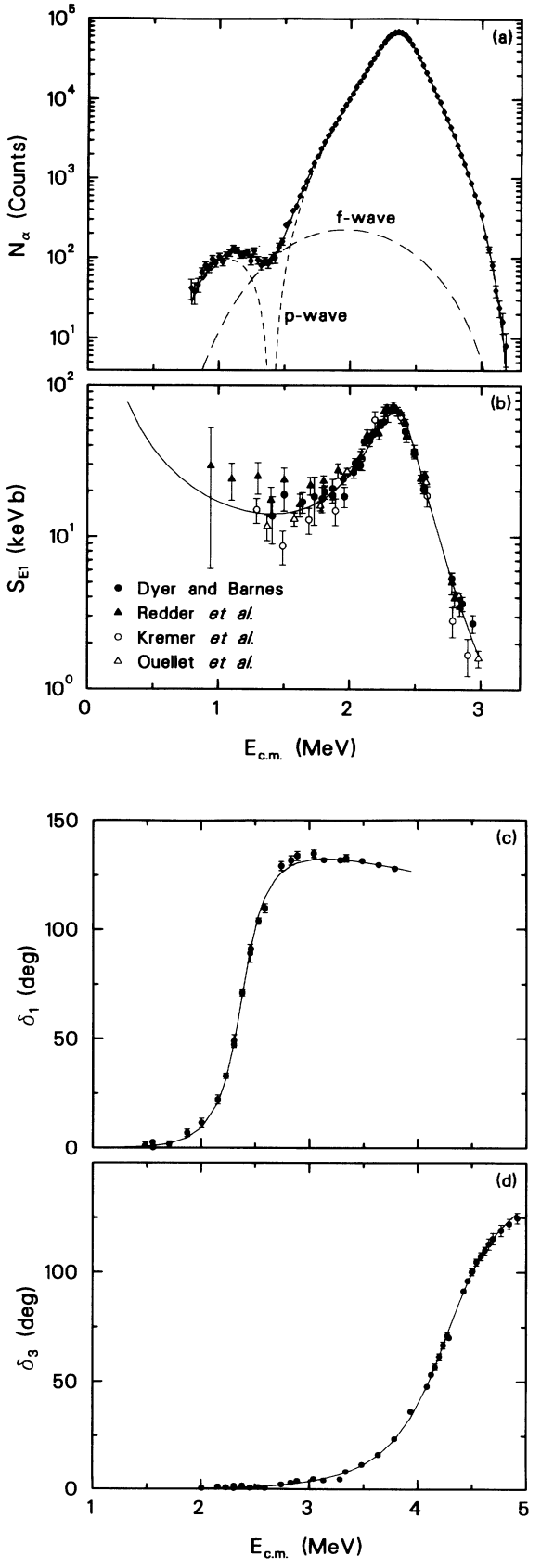

FIG. 19. R-matrix fits to data for overall best-fit parameter values given in Table III. (a) ^{16}N β-decay-delayed α spectrum; (b) ^{12}C$(\alpha,\gamma)^{16}$O $E1$ S factor; (c) ^{12}C + α $\ell = 1$ phase shift; (d) ^{12}C + α $\ell = 3$ phase shift.

ground terms B_{32} and $b_{3\beta\alpha}$. If we set both parameters to zero, the value of $\chi^2_{\rm min}$ is increased by 4, $S_{E1}(300)$ is changed by less than 1 keV b, and the acceptable range of $S_{E1}(300)$ is reduced from ± 19 to ± 16 keV b compared with values obtained with B_{32} and $b_{3\beta\alpha}$ as variables. Thus, for the same reason that we fixed the R-matrix f-wave parameters $A_{23} = A_{33} = 0$, we take $B_{32} = b_{3\beta\alpha} = 0$ for our K-matrix analysis.

The dependence of χ^2 and $S_{E1}(300)$ on the energy E_{13} of the p-wave background term is shown in Figs. 20(a) and (b), respectively. Since neither quantity changes significantly for $E_{13} > 100$ MeV, we adopt the value $E_{13} = 100$ MeV for our final fits.

Results of simultaneous fits to all the data are presented in Table IV, which gives the best-fit value $S_{E1}(300) = 82 \pm 16$ keV b. K-matrix plots corresponding to Fig. 19 are not included as they are similar to their R-matrix counterparts. This value was determined from the minimum of the curve χ^2 versus $S_{E1}(300)$, which is presented in Fig. 21. Also plotted are the values of different components of the total χ^2. The uncertainty in the S factor has been determined using the criterion described in Sec. III C.

F. Interference sign for the radiative capture reaction

In the previous literature (e.g., [11,17]), there was some discussion concerning the sign of the interference term in the energy region between the two 1^- states in the $^{12}C(\alpha,\gamma)^{16}O$ cross section. For fits utilizing the com-

TABLE III. Best-fit R-matrix parameters at $a = 6.5$ fm with $A_{23} = A_{33} = 0$. Quantities in parentheses denote fixed input values; values in brackets are calculated from a fixed input and one fitted parameter ($\gamma_{1\ell}$). The first column shows parameter values with the boundary condition $[B_\ell = S_\ell(E_{1\ell})]$ set equal to the shift function at the subthreshold level. The second column gives parameter values for each level λ corresponding to $B_\ell = S_\ell(E_{\lambda\ell})$.

	$B_\ell = S_\ell(E_{1\ell})$	$B_\ell = S_\ell(E_{\lambda\ell})$
E_{11} (MeV)	(−0.0451)	(−0.0451)
γ_{11} (MeV$^{1/2}$)	0.0793	0.0793
$\gamma_{1\gamma}$ (MeV^{-1})	[8.761×10^{-6}]	[8.761×10^{-6}]
$A_{11}/\sqrt{N_\alpha}$ (MeV$^{1/2}$)[a]	[0.0947]	[0.0947]
E_{21} (MeV)	2.845	2.400
γ_{21} (MeV$^{1/2}$)	0.330	0.471
$\gamma_{2\gamma}$ (MeV^{-1})	-2.439×10^{-6}	-3.196×10^{-6}
$A_{21}/\sqrt{N_\alpha}$ (MeV$^{1/2}$)[a]	0.184	0.192
$\Gamma^{\rm obs}_{21}$ (MeV)	b	0.359
E_{31} (MeV)	11.71	7.999
γ_{31} (MeV$^{1/2}$)	1.017	0.912
$\gamma_{3\gamma}$ (MeV^{-1})	-2.819×10^{-6}	-2.498×10^{-6}
$A_{31}/\sqrt{N_\alpha}$ (MeV$^{1/2}$)[a]	−0.640	−0.712
$\Gamma^{\rm obs}_{31}$ (MeV)	b	9.04
E_{13} (MeV)	(−1.032)	(−1.032)
γ_{13} (MeV$^{1/2}$)	0.0765	0.0765
$A_{13}/\sqrt{N_\alpha}$ (MeV$^{1/2}$)[a]	[0.192]	[0.192]
E_{23} (MeV)	4.798	4.242
γ_{23} (MeV$^{1/2}$)	0.251	0.497
$A_{23}/\sqrt{N_\alpha}$ (MeV$^{1/2}$)[a]	0	−0.0390
$\Gamma^{\rm obs}_{23}$ (MeV)	b	0.757
E_{33} (MeV)	17.71	9.988
γ_{33} (MeV$^{1/2}$)	1.244	1.115
$A_{33}/\sqrt{N_\alpha}$ (MeV$^{1/2}$)[a]	0.0	−0.115
$\Gamma^{\rm obs}_{33}$ (MeV)	b	13.68
$S_{E1}(300)$ (keV b)	79 ± 16[c]	
χ^2_β ($N = 87$)	100	
$\chi^2_{\delta 1}$ ($N = 26$)	32.8	
$\chi^2_{\delta 3}$ ($N = 40$)	59.8	
χ^2_γ ($N = 71$)	184	
$\chi^2_{\rm min}$ ($N = 224$)	377	

[a]Division by $\sqrt{N_\alpha} = (1.0265\times10^6)^{1/2}$ removes the dependence of the values of these parameters on the number of α counts collected.
[b]Not applicable.
[c]Systematic error not included.

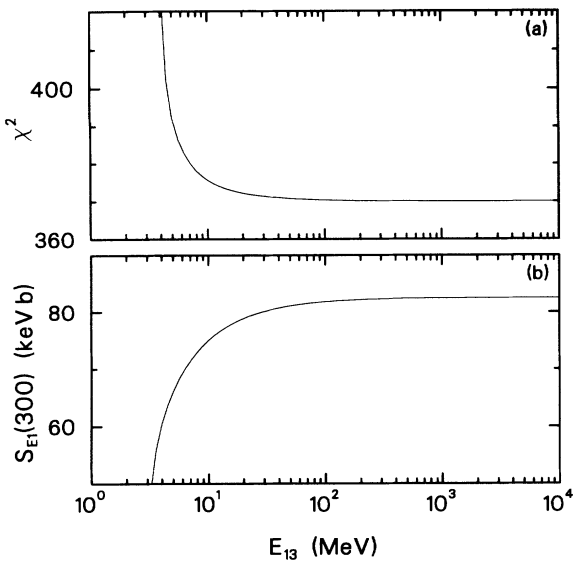

FIG. 20. (a) χ^2 and (b) the corresponding $S_{E1}(300)$ as functions of E_{13}.

bined σ_{E1} data of Sec. III E, the minimum χ^2 occurred with constructive interference. However, local minima of χ^2 do exist for which the interference term is destructive between the states.

In the R-matrix calculations two such solutions occur: one at $a = 7$ fm and $S_{E1}(300) = 4$ keV b with a minimum $\chi^2 = 467$; and a second at $a = 8.5$ fm and $S_{E1}(300) = 0$ keV b with $\chi^2 = 464$. These two local minima can be seen in the contour plot of Fig. 16 along with the absolute minimum at $a = 6.5$ fm and $S_{E1}(300) = 79$ keV b for which $\chi^2 = 376$. Due to the increased χ^2, these solutions for destructive interference were ruled out. Similarly, a local minimum is found in the K-matrix fit at $S_{E1}(300) = 8$ keV b with a χ^2 of 397 (Fig. 21), which is larger than the value of $\chi^2_{\min} = 370$ obtained at $S_{E1}(300) = 82$ keV b.

It is concluded that the possibility of destructive interference in the region between the two 1^- states in the $^{12}C(\alpha,\gamma)^{16}O$ reaction is excluded at about the 5σ level by the R-matrix fits. The large increase in the values of χ^2 for the destructive interference solutions (see above) stems from the poor fit to the radiative capture data. The reason for this is that the deep interference minimum for the radiative capture fit is forced to an energy near the low-energy data points by the large value of the reduced width of the subthreshold state required in the fit to the $^{16}N(\beta\alpha)$ data.

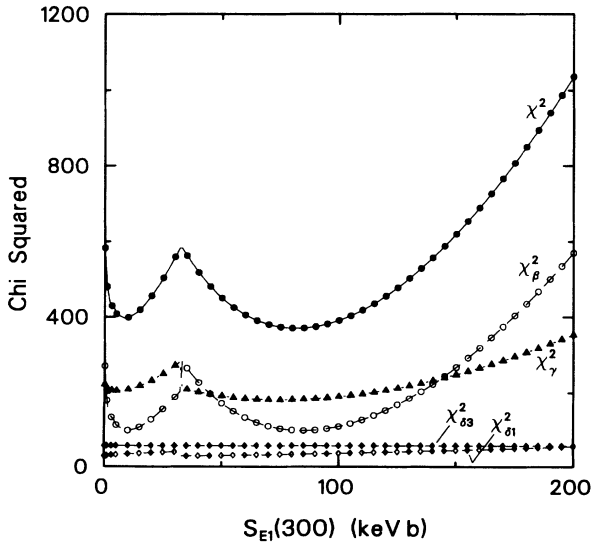

FIG. 21. Variation of χ^2 and its components with $S_{E1}(300)$ for the best K-matrix fit. See text for details.

G. Systematic errors

Systematic errors were estimated by repeating the analysis under conditions in which each factor that might lead to uncertainty was varied independently and the change in $S_{E1}(300)$ determined. For the R-matrix fits, variations were carried out only with the optimum channel radius of $a = 6.5$ fm.

Among the various external measurements used to fix some of the fitting parameters of the subthreshold states, the most significant uncertainty was found to arise from the relative β-branching ratio to the two 1^- states (see also Ref. [18]). This ratio determines the parameters A_{11} and B_{11} used in the R- and K-matrix analyses, respectively. The $\pm 9\%$ uncertainty in its value leads to a range of ± 6 keV b in the extrapolated S factor. The $\pm 6\%$ uncertainty in the gamma width of the $E_x = 7.117$ MeV state, used to calculate $\gamma_{1\gamma}$ and $g_{1\gamma 1}$, introduces an error of ± 2 keV b in the K-matrix analysis and ± 3 keV b in the R-matrix analysis. Uncertainties in the energies of the subthreshold states have a negligible effect on the final $S_{E1}(300)$.

The four $^{12}C(\alpha,\gamma)^{16}O$ data sets show obvious systematic differences. An estimate of the error arising from these differences can be obtained from the observed spread in the S factors obtained when each data set is used separately in the fit. This procedure is discussed in more detail in Sec. III J where the results of separate fits are presented in Tables V and VI. From these tables, the systematic errors are assumed to be ± 4 keV b for the R-matrix results and ± 16 keV b for the K-matrix results. The $\pm 10\%$ uncertainty in the overall normalization of the (α,γ) cross section data contributes an additional ± 2 keV b in both types of analyses.

Several systematic effects in the ^{16}N spectrum also affect the final S-factor result. The $\pm 10\%$ uncertainty in the amount of ^{18}N contamination causes an uncertainty of ± 1 keV b, while the effect of the subtraction of the response tail was found to be negligible. The quoted uncertainty of $^{+2500}_{-1000}$ counts in the ^{17}N contribution of 1500 counts (see Sec. II D 4) results in an uncertainty in $S_{E1}(300)$ of about ± 5 keV b in the R-matrix fits, and ± 1 keV b in the K-matrix fits. Variations of ± 5 keV in the energy resolution give errors of ± 2 keV b. A reduction in coincidence efficiency by the amount quoted in Sec.

TABLE IV. Best-fit K-matrix parameters. The convention of Refs. [18,34,41,42] is followed here in multiplying parameters by powers of $a = 5.46$ fm to produce units of MeV or MeV$^{1/2}$.

E_{11} (MeV)	(-0.0451)[a]
$g_{1\alpha 1}a^{-3/2}$ (MeV$^{1/2}$)	-7.122
$g_{1\gamma 1}a^{-3/2}$ (MeV$^{1/2}$)	(1.897×10^{-3})[b]
$B_{11}/\sqrt{N_\alpha}$[c]	(1.21)[d]
E_{12} (MeV)	2.451
$g_{1\alpha 2}a^{-3/2}$ (MeV$^{1/2}$)	6.939
$g_{1\gamma 2}a^{-3/2}$ (MeV$^{1/2}$)	0.6647×10^{-3}
$B_{12}/\sqrt{N_\alpha}$[c]	-0.4217
$\Gamma_{1\alpha 2}$ (MeV)[e]	0.454
E_{13} (MeV)	(100)
$g_{1\alpha 3}a^{-3/2}$ (MeV$^{1/2}$)	$-342.3i$
$g_{1\gamma 3}a^{-3/2}$ (MeV$^{1/2}$)	$-19.58 \times 10^{-3}i$
$B_{13}/\sqrt{N_\alpha}$[c]	$21.18i$
$b_{1\alpha\alpha}a^{-3}$	1248
$b_{1\gamma\alpha}a^{-3}$	67.94×10^{-3}
$b_{1\beta\alpha}a^{-3/2}/\sqrt{N_\alpha}$(MeV$^{-1/2}$)[c]	-76.68
E_{31} (MeV)	(-1.032)
$g_{3\alpha 1}a^{-7/2}$ (MeV$^{1/2}$)	0.06202
$B_{31}/\sqrt{N_\alpha}$[c]	(2.50)[d]
E_{32} (MeV)	4.414
$g_{3\alpha 2}a^{-7/2}$ (MeV$^{1/2}$)	0.06478
$B_{32}/\sqrt{N_\alpha}$[c]	(0)
$\Gamma_{3\alpha 2}$ (MeV)[e]	0.944
E_{33} (MeV)	(15)
$g_{3\alpha 3}a^{-7/2}$ (MeV$^{1/2}$)	$-0.4538i$
$B_{33}/\sqrt{N_\alpha}$[c]	(0)
$b_{3\alpha\alpha}a^{-7}$	0.02323
$b_{3\beta\alpha}a^{-7/2}/\sqrt{N_\alpha}$(MeV$^{-1/2}$)[c]	(0)
$S_{E1}(300)$ (keV b)	82 ± 16[f]
χ^2_β ($N = 87$)	97.8
$\chi^2_{\delta 1}$ ($N = 26$)	33.9
$\chi^2_{\delta 3}$ ($N = 40$)	57.0
χ^2_γ ($N = 71$)	181.6
$\chi^2_{\min}$ ($N = 224$)	370

[a]Numbers in parentheses are fixed.
[b]From $\Gamma_{1\gamma 1} = 2p^2_{1\gamma}(E_{11})g^2_{1\gamma 1} = 55$ meV.
[c]Division by $\sqrt{N_\alpha} = (1.0265 \times 10^6)^{1/2}$ removes the dependence of the values of these parameters on the number of α counts collected.
[d]B_{11} and B_{31} fixed from branching ratios.
[e]$\Gamma_{\ell\alpha\lambda} = 2p^2_{\ell\alpha}(E_{\ell\lambda})g^2_{\ell\alpha\lambda}$.
[f]Systematic error not included.

TABLE V. R-matrix fits to the four separate ^{12}C$(\alpha,\gamma)^{16}$O data sets as well as to a combined set at $a = 6.5$ fm.

	N_γ	χ^2_ν	χ^2_β ($N = 87$)	$\chi^2_{\delta 1}$ ($N = 26$)	$\chi^2_{\delta 3}$ ($N = 40$)	χ^2_γ	$S_{E1}(300)$ (keV b)
Ref. [7]	24	1.47	99.0	33.3	59.8	46.5	(77)[a]
Ref. [9]	26	1.45	98.8	33.3	59.8	45.2	(87)[a]
Ref. [10]	12	1.41	98.5	33.6	59.8	19.1	(79)[a]
Ref. [11]	9	1.47	99.3	33.0	59.7	24.0	(80)[a]
All	71	1.80	100.0	32.8	59.7	184.0	79 ± 16[b]

[a] Nonfinal values for $S_{E1}(300)$ which are quoted for comparison purposes are enclosed in parentheses.
[b]Systematic error not included.

TABLE VI. K-matrix fits to the four separate $^{12}C(\alpha,\gamma)^{16}O$ data sets as well as to the combined set.

	N_γ	χ^2_ν	χ^2_β ($N=87$)	$\chi^2_{\delta 1}$ ($N=26$)	$\chi^2_{\delta 3}$ ($N=40$)	χ^2_γ	$S_{E1}(300)$ (keV b)
Ref. [7]	24	1.36	97.1	34.3	57.0	29.9	(94)[a]
Ref. [9]	26	1.38	97.0	34.4	57.0	35.8	(99)[a]
Ref. [10]	12	1.33	96.9	34.4	57.0	10.2	(66)[a]
Ref. [11]	9	1.44	97.4	34.1	57.0	21.9	(74)[a]
All	71	1.78	97.8	33.9	57.0	181.6	82 ± 16[b]

[a]Nonfinal values for $S_{E1}(300)$ which are quoted for comparison purposes are enclosed in parentheses.
[b]Systematic error not included.

II D 6 caused a maximum change of +3 keV b, while the possible presence of noise events in the spectrum (Sec. II D 7) leads to a change of −1 keV b. Uncertainties in the energy calibration for the ^{16}N data lead to an estimated ±10 keV b error in $S_{E1}(300)$. Adding all of these contributions in quadrature, we obtain a systematic error of ±14 keV b for the R-matrix and ±20 keV b for the K-matrix fits.

As an additional test of the stability of the R- and K-matrix fits with respect to the α spectrum, analyses were carried out which exclude all the data points in the region of the interference minimum from $E_\alpha = 0.86$ MeV to 1.37 MeV. This procedure resulted in only very small changes in the extracted values of $S_{E1}(300)$ (+4 keV b for the R-matrix fits and +1 keV b for the K-matrix fits) with no significant changes in χ^2_ν.

H. Comparison with the R-matrix fits of Refs. [13,31,32]

The present work follows closely the procedures of Ref. [13]. However, some of the *a priori* restrictions on the p-wave parameters assumed in the previous works [13,31,32] were relaxed to allow a good fit to the data now available. In particular, the fits need a considerable feeding both in the radiative capture as well as the β-channel for the p-wave background state. Similar restrictions to those used previously were placed on the f-wave parameters, for the reasons stated in Sec. III E 1. A slightly higher channel radius than the commonly used value of $a = 5.5$ fm is confirmed as was proposed in Ref. [31].

References [13,31,32] used a spectrum in their fits which had been constructed from data based on a private communication [33] between Wäffler and Barker. In this spectrum only every fourth point was taken and the error bars were extended beyond the purely statistical to incorporate systematic errors from the energy calibration. Therefore a χ^2 per degree of freedom far below unity [34] can be found for fits to this spectrum. For this reason, the χ^2 values of the previous works [13,31,32] and of the present are not directly comparable. We have reconstructed a spectrum from the private communication (see Fig. 15 and Sec. II E 1) and find it difficult to fit even with the subtraction of a response-function tail comparable to that in the present work.

I. Comparison with the K-matrix fits of Refs. [19,34]

The final value of the S factor in the present work is $S_{E1}(300) = 82$ keV b for the background state energy $E_{13} = 100$ MeV, compared with our preliminary results of $S_{E1}(300) = 57$ keV b and 68 keV b for $E_{13} = 7$ MeV and 20 MeV, respectively [19]. In Ref. [34], which used the same α spectrum as Ref. [19], a value of $S_{E1}(300) = 42$ keV b was found for $E_{13} = 8$ MeV.

The analyses of both Refs. [19,34] use the same parametrization, but Ref. [34] employs only one $\sigma_{E1}(\alpha,\gamma)$ data set [10] while Ref. [19] uses all four measurements. In addition, Ref. [34] makes use of the $\ell = 1$ and 3 phase shifts which were not used in Ref. [19].

Also, the two studies use different goodness-of-fit criteria for χ^2, which affects only the size of the quoted errors. We have verified that the method of analysis described in Ref. [19] gives identical results to those of Ref. [34] if carried out under the same conditions. We regard both sets of results as preliminary.

The result of the present work differs from that in Ref. [19] in several respects. Firstly, refinements in the data analysis have led to a final spectrum which has mi-

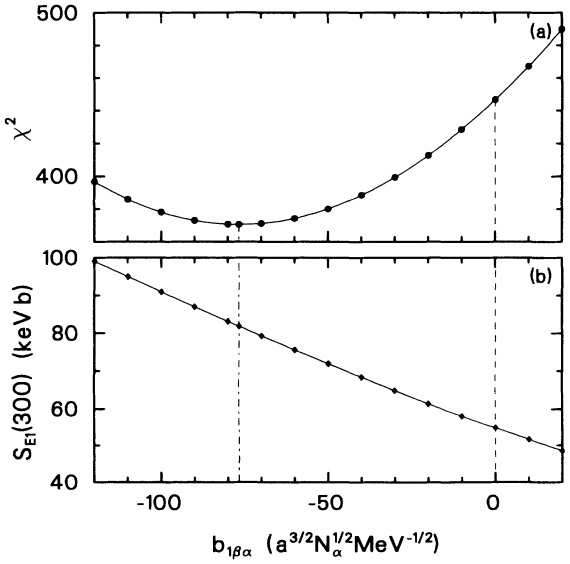

FIG. 22. Dependence on $b_{1\beta\alpha}$ of (a) χ^2 and (b) $S_{E1}(300)$. See text for discussion.

nor differences from that employed in Ref. [19] (mainly in the energy calibration). Secondly, the $\ell = 1$ and $\ell = 3$ phase shifts of Ref. [35] were employed in simultaneous fits, even though the inclusion of the $\ell = 3$ data leads to an insignificant change in the value of $S_{E1}(300)$. Finally, the present work includes an additional p-wave background parameter, $b_{1\beta\alpha}$, which was absent in Refs. [19,34], and E_{13} was increased to 100 MeV. The inclusion of these changes was found to be important in order to obtain good fits to the improved ^{16}N $\beta\alpha$ spectrum. This is illustrated in Fig. 22 where χ^2 and $S_{E1}(300)$ are shown as functions of $b_{1\beta\alpha}$. The dot-dashed lines indicate the value of $\chi^2_{\rm min}$ and the corresponding $S_{E1}(300)$ of the present work. The dashed lines indicate values of χ^2 and $S_{E1}(300)$ that would be obtained if $b_{1\beta\alpha}$ were set equal to zero.

Since the final uncertainties of the present work are based on a different goodness-of-fit criterion for χ^2, it is not meaningful to make a direct comparison of the present uncertainties with those of Refs. [19,34].

J. The influence of different radiative capture sets on the final result

As mentioned earlier, the four sets of ^{12}C$(\alpha,\gamma)^{16}$O measurements [7,9–11] display clear systematic differences. After combining the four σ_{E1} measurements into a single data set, comparable values for $S_{E1}(300)$ are obtained in both R- and K-matrix analyses. It is therefore assumed that the differences in the σ_{E1} measurements contribute primarily to the systematic error in $S_{E1}(300)$.

Analyses have been performed separately for each σ_{E1} data set; the results are shown in Tables V and VI for the R- and K-matrix calculations, respectively. The results presented in Table V yield a spread of ± 4 keV b for $S_{E1}(300)$, considerably smaller than the ± 16 keV b spread from the K-matrix values in Table VI. This is because the parametrization for the radiative capture channel in the R-matrix formulation is more restrictive than that for the K matrix; i.e., the K-matrix parametrization includes an additional parameter $b_{1\gamma\alpha}$. If the K-matrix parameter space is restricted to be more nearly comparable to that of the R matrix (by taking $b_{1\gamma\alpha} = 0$, for example) the resultant spread in $S_{E1}(300)$ is comparable to that of the R matrix. On the other hand, if the R-matrix parametrization is expanded to include a fourth state, a spread somewhat larger than that for the K matrix is found. It appears that the exact choice of parametrization for the background terms in the (α,γ) channel has a significant effect on the systematic error to be assigned. We note, however, that the average value of $S_{E1}(300)$ for the separate fits is in each case always very close to that obtained for the corresponding fit to the combined (α,γ) data set. This supports our choice in using the combined data set to find the most trustworthy value for $S_{E1}(300)$. Furthermore, as our stated intention was to confine our analyses, so far as possible, to parametrizations already established in the literature, we take the spreads in Tables V and VI to be appropriate estimates of the systematic errors.

IV. SUMMARY AND CONCLUSIONS

In the present work a measurement of the β-delayed α spectrum of ^{16}N is reported which has been carried out, for the first time, in conjunction with an experimental determination of the complete response function of the detection system. In addition, the energy range of the spectrum has been extended beyond a previous measurement [14] showing a low-energy structure that is most likely produced by the p-wave interference between the $E_x = 7.117$ and 9.59 MeV 1^- states in ^{16}O. In the β-delayed α spectrum, this interference is destructive in the energy region between the states.

The ^{16}N spectrum obtained here has been employed in R- and K-matrix fits, together with the ^{12}C$(\alpha,\gamma)^{16}$O data and the elastic-scattering data for α particles on ^{12}C, to derive $S_{E1}(300)$, the $E1$ S factor of the ^{12}C$(\alpha,\gamma)^{16}$O reaction at $E = 300$ keV.

The R-matrix fits to the data result in

$$S_{E1}(300) = 79 \pm 21 \text{ keV b}, \tag{17}$$

using the model space discussed in Secs. III D 1 and III E 1; statistical and systematic errors have been added in quadrature.

The K-matrix fits to the data result in

$$S_{E1}(300) = 82 \pm 26 \text{ keV b} \tag{18}$$

for the model space discussed in Secs. III D 2 and III E 2; statistical and systematic errors have been added in quadrature.

The final S factors are close to one another and well within the errors, whereas in previous work the K-matrix results were usually lower. This is the first time that both R- and K-matrix analyses have been carried out concurrently using a β-delayed α spectrum covering a broad range of energies. It is not surprising then that some of the discrepancies between the values obtained in other separate R- and K-matrix calculations are absent here.

With the much improved S-factor curve for the $E1$ cross section, it may now be possible to derive more accurate values from the γ-ray angular distributions of Refs. [9,11] for the cross section of the $E2$ transitions to the ground state of ^{16}O. From these improved $E2$ cross sections and from new measurements in progress [45], a more precise determination of $S(300)$ should become possible.

ACKNOWLEDGMENTS

We would like to express our appreciation to J. Humblet for extensive help and advice given to us in the development of our K-matrix analysis. This contribution proved to be invaluable. We wish to thank E.W. Vogt for valuable discussions concerning the R-matrix analysis. We also wish to thank H. Biegenzein, D. Jones, P. Machule, H. Sprenger, A. Wilson, and G. Sheffer for help with the technical aspects of the experiment, and D. Diel and P. W. Green for assistance with the data acquisition

system. Our special thanks go to Teleglobe Canada for the donation of a 6 GHz amplifier, without which the operation of the ECR source at TISOL and this experiment would have been impossible. The help of summer students A. Chen, J. Chen, and M. Trinczek is gratefully acknowledged. One of the authors (R.E.A.) wishes to express his thanks to the Kellogg Radiation Laboratory at Caltech for their hospitality during the early stages of the experiment. This work was supported in part by the Natural Sciences and Engineering Research Council of Canada, by the National Science Foundation (Grant No. PHY-91-15574), and by TRIUMF.

[1] W.A. Fowler, Rev. Mod. Phys. **56**, 149 (1984).
[2] T.A. Weaver and S.E. Woosley, Phys. Rep. **227**, 65 (1993).
[3] C.E. Rolfs and W.S. Rodney, *Cauldrons in the Cosmos* (University of Chicago Press, Chicago, 1988), p. 387.
[4] F. Ajzenberg-Selove, Nucl. Phys. **A460**, 1 (1986); **A471**, 1 (1987); D.R. Tilley, H.R. Weller, and C.M. Cheves, *ibid.* **A564**, 1 (1993).
[5] R.J. Jaszczak, J.H. Gibbons, and R.L. Macklin, Phys. Rev. C **2**, 63 (1970).
[6] R.J. Jaszczak and R.L. Macklin, Phys. Rev. C **2**, 2452 (1970).
[7] P. Dyer and C.A. Barnes, Nucl. Phys. **A233**, 495 (1974).
[8] K.U. Kettner, H.W. Becker, L. Buchmann, J. Görres, H. Kräwinkel, C. Rolfs, P. Schmalbrock, H.P. Trautvetter, and A. Vlieks, Z. Phys. A **308**, 73 (1982).
[9] A. Redder, H.W. Becker, C. Rolfs, H.P. Trautvetter, T.R. Donoghue, T.C. Rinckel, J.W. Hammer, and K. Langanke, Nucl. Phys. **A462**, 385 (1987).
[10] R.M. Kremer, C.A. Barnes, K.H. Chang, H.C. Evans, B.W. Filippone, K.H. Hahn, and L.W. Mitchell, Phys. Rev. Lett. **60**, 1475 (1988).
[11] J.M.L. Ouellet, H.C. Evans, H.W. Lee, J.R. Leslie, J.D. MacArthur, W. McLatchie, H.-B. Mak, P. Skensved, J.L. Whitton, X. Zhao, and T.K. Alexander, Phys. Rev. Lett. **69**, 1896 (1992).
[12] C. Werntz, Phys. Rev. C **4**, 1591 (1971).
[13] F.C. Barker, Aust. J. Phys. **24**, 777 (1971).
[14] K. Neubeck, H. Schober, and H. Wäffler, Phys. Rev. C **10**, 320 (1974); H. Hättig, K. Hünchen, and H. Wäffler, Phys. Rev. Lett. **25**, 941 (1970).
[15] E.L. Sprenkel-Segel, R.E. Segel, and R.H. Siemssen, in *Proceedings of the Third International Conference on High-Energy Physics and Nuclear Structure*, Columbia University, 1969, edited by S. Devons (Plenum, New York, 1970), p. 763.
[16] D. Baye and P. Descouvemont, Nucl. Phys. **A481**, 445 (1988).
[17] X. Ji, B.W. Filippone, J. Humblet, and S.E. Koonin, Phys. Rev. C **41**, 1736 (1990).
[18] J. Humblet, B.W. Filippone, and S.E. Koonin, Phys. Rev. C **44**, 2530 (1991).
[19] L. Buchmann, R. E. Azuma, C. A. Barnes, J. M. D'Auria, M. Dombsky, U. Giesen, K. P. Jackson, J. D. King, R.G. Korteling, P. McNeely, J. Powell, G. Roy, J. Vincent, T.R. Wang, S. S. M. Wong, and P. R. Wrean, Phys. Rev. Lett. **70**, 726 (1993).
[20] Z. Zhao, R.H. France III, K.S. Lai, S.L. Rugari, M. Gai, and E.L. Wilds, Phys. Rev. Lett. **70**, 2066 (1993).
[21] M. Dombsky, J.M. D'Auria, L. Buchmann, H. Sprenger, J. Vincent, P. McNeely, and G. Roy, Nucl. Instrum. Methods **A295**, 291 (1990).
[22] L. Buchmann, J. Vincent, H. Sprenger, M. Dombsky, J.M. D'Auria, P. McNeely, and G. Roy, Nucl. Instrum. Methods **B62**, 521 (1992).
[23] M. Dombsky, L. Buchmann, J.M. D'Auria, P. McNeely, G. Roy, H. Sprenger, and J. Vincent, Nucl. Instrum. Methods **B70**, 125 (1992).
[24] J.F. Ziegler, J. Biersack, and U. Littmark, *Code* TRIM85, *The Transport of Ions in Solids* (Pergamon, New York, 1985).
[25] K.I. Hahn, C.R. Brune, and P.R. Wrean, Phys. Rev. C **48**, 914 (1993).
[26] E.T.H. Clifford, E. Hagberg, J.C. Hardy, H. Schmeing, R.E.Azuma, H.C. Evans, V.T. Koslowsky, U.J. Schrewe, K.S. Sharma, and I.S. Towner, Nucl. Phys. **A493**, 293 (1989).
[27] L. Buchmann, R. E. Azuma, C. A. Barnes, J. M. D'Auria, M. Dombsky, U. Giesen, K. P. Jackson, J. D. King, R. Korteling, P. McNeely, J. Powell, G. Roy, J. Vincent, S. S. M. Wong, and P. R. Wrean, Nucl. Instrum. Methods **B79**, 330 (1993).
[28] M. Dombsky, L. Buchmann, J.M. D'Auria, U. Giesen, K.P. Jackson, J.D. King, E. Korkmaz, R.G. Korteling, P. McNeely, J. Powell, G. Roy, M. Trinczek, and J. Vincent, Phys. Rev. C **49**, 1867 (1994).
[29] M.J.G. Borge, H. Cronberg, M. Cronqvist, H. Gabelmann, P.G. Hansen, L. Johannsen, B. Jonson, S. Mattsson, G. Nyman, A. Richter, K. Riisager, O. Tengblad, and M. Tomaselli, Nucl. Phys. **A490**, 287 (1988).
[30] J. Powell, Ph.D thesis, University of Toronto, 1994.
[31] F.C. Barker and T. Kajino, Aust. J. Phys. **44**, 369 (1991).
[32] F.C. Barker, Aust. J. Phys. **40**, 25 (1987).
[33] H. Wäffler to F.C. Barker (private communication).
[34] J. Humblet, B.W. Filippone, and S.E. Koonin, Phys. Rev. C **48**, 2114 (1993).
[35] R. Plaga, H.W. Becker, A. Redder, C. Rolfs, H.P. Trautvetter, and K. Langanke, Nucl. Phys. **A465**, 291 (1987).
[36] C.M. Jones, G.C. Phillips, R.W. Harris, and E.H. Beckner, Nucl. Phys. **37**, 1 (1962).
[37] G.J. Clark, D.J. Sullivan, and P.B. Treacy, Nucl. Phys. **A110**, 481 (1968).
[38] "MINUIT, Function Minimization and Error Analysis," CERN Program Library Entry D506 (unpublished).
[39] E.J. Konopinski and M.E. Rose, in *Alpha, Beta, and Gamma Ray Spectroscopy II*, edited by K. Siegbahn (North-Holland, Amsterdam, 1966), p. 1327.
[40] A.M. Lane and R.G. Thomas, Rev. Mod. Phys. **30**, 257 (1958).
[41] J. Humblet, P. Dyer, and B.A. Zimmerman, Nucl. Phys. **A271**, 210 (1976).
[42] B.W. Filippone, J. Humblet, and K. Langanke, Phys. Rev. C **40**, 515 (1989).
[43] J. Humblet, Phys. Rev. C **42**, 1582 (1990).
[44] F.C. Barker, Aust. J. Phys. **25**, 341 (1972).
[45] C. Rolfs (private communication).

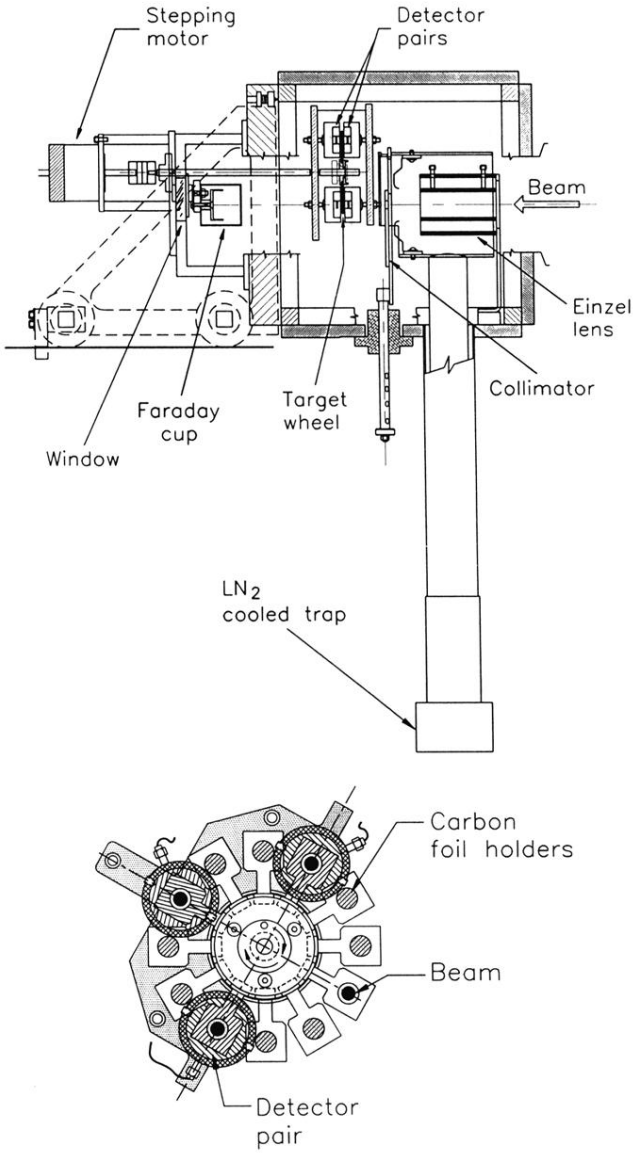

FIG. 2. Top—diagram of the target chamber assembly in the plane containing the beam. Bottom—target wheel showing the implantation foils and detector locations.